Physics of Fluids, Volume 36, Issue 4, April 2024, Article number 045112
DOI:10.1063/5.0196979

Experimental and Numerical Investigation of the Aerodynamic Characteristics of High-Performance Vehicle Configurations Under Yaw Conditions

Steven Rijns[a,*], Tom-Robin Teschner[b], Kim Blackburn[a], Anderson Ramos Proenca[c], James Brighton[a]

[a]*Advanced Vehicle Engineering Centre, Cranfield University, Cranfield, MK43 0AL, United Kingdom*
[b]*Centre for Computational Engineering Sciences, Cranfield University, Cranfield, MK43 0AL, United Kingdom*
[c]*Centre for Aeronautics, Cranfield University, Cranfield, MK43 0AL, United Kingdom*

Abstract

This study investigates the impact of yaw conditions on the aerodynamic performance and flow field of three high-performance vehicle model configurations by means of wind tunnel testing and Unsteady Reynolds-Averaged Navier-Stokes (URANS) based computational fluid dynamics (CFD) simulations. While yaw effects on automotive vehicles have been explored, the effects on far more complex flow fields of high-performance vehicles remain insufficiently researched. This paper reveals that yaw conditions have a significant negative influence both downforce and drag performance. Spoiler and rear wing devices enhance downforce but increase the vehicle's sensitivity to yaw. Furthermore, yaw conditions significantly alter vortex structures and local flow velocities, affecting downstream flow behaviour. Surface pressure measurements on the slant confirm these findings, and highlight notable yaw effects and upstream effects from spoiler and rear wing devices. Wake analyses through total pressure measurements shows that yaw induces a substantial deviation from straight-line wake characteristics, which become dominated by an inboard rotating vehicle body vortex. Overall, this research enhances the understanding of the effects of yaw conditions on high-performance vehicle aerodynamics and provides valuable data for future vehicle aerodynamics research in real-world operating conditions.

Keywords:
Aerodynamics, High-Performance Vehicles, Yaw, Wind tunnel, DrivAer, CFD

1. Introduction

Aerodynamic research plays an important role in optimising vehicle efficiency and performance in automotive and motorsport industries. Vehicles operate in a wide range of dynamic conditions such as yaw and cornering, which influences their aerodynamic performance. This is especially true for high-performance vehicles, which rely on significant downforce generation to improve tractive forces. However, the majority of published vehicle aerodynamics research is focussed on straight-line conditions, providing only limited insights on real driving scenarios.

Available studies which consider more dynamic conditions have looked at the effects of yaw conditions on simplified automotive bodies. Findings generally showed a substantial exponential drag increase as a function of yaw angle [3,25,36,10,30,6]. While most of the analyses were limited to the effects on drag, some studies showed that lift experienced a stronger exponential increase with yaw angle [36,6,23,15,39]. The experimental setup and vehicle model mounting systems in these studies demonstrated to be influential on the vehicle's yaw sensitivity, indicating the significance of underbody airflow on the aerodynamic performance of these simplified bodies.

*Corresponding author at: Advanced Vehicle Engineering Centre, Cranfield University, Cranfield, MK43 0AL, United Kingdom.
Email address: steven.rijns@cranfield.ac.uk

The considerable impact of yaw conditions on their aerodynamic performance was attributed to variations in the flow field [4,37,19,25,23,36,15]. Yaw conditions introduced a windward pressure build-up, resulting in a leeward acting side force which increased fairly linearly with yaw angle. The formation of vortices enhanced along the sharp edges of the windward roofline, windward c-pillar and leeward roofline. The angled oncoming flow also increased flow separation along the leeward side of the vehicle, and gave rise to the formation of a vortex along the leeward edge of the underbody. Furthermore, yaw conditions increased flow attachment along the slant, but also created significant low pressure concentrations on the leeward side of the vehicle's base. These low pressure concentrations resulted from recirculation zones on the leeward side of the wake, which were drawn towards the dominant wake structure from the windward c-pillar vortex.

The discrepancies between these studies and research on more realistic passenger vehicle geometries [26,45,33,41,12] indicate that findings on simplified automotive bodies are not directly applicable on more complex vehicle geometries. Investigations on passenger vehicles showed that drag increased fairly linearly from about 0° to 10° yaw, after which the drag increments levelled off. Lift generation initially slightly reduced at yaw angles smaller than 4°, beyond which lift generation started to increase exponentially. The side force demonstrated a more comparable yaw sensitivity to the findings on simplified automotive bodies, where it increased fairly linearly in the leeward

direction with yaw.

The effects of yaw conditions on the flow field of realistic passenger vehicles generally showed a suppression of the windward a-pillar (roofline) vortex and the leeward c-pillar vortex[42,45,7,38,41,12,22]. On the other hand, the strength of leeward a-pillar vortex significantly increased with yaw and propagated further outboard. The strength of the windward c-pillar vortex varied between different rear end geometries, but they all demonstrated a dominant inboard rotating wake vortex generated at the windward side of the vehicle yaw.

The existing research has provided valuable insights into yaw effects on simplified automotive bodies and passenger vehicles. However, high-performance vehicles feature additional downforce-generating aerodynamic elements like rear wings, spoilers, diffusers and splitters. Studies have indicated that these elements can significantly improve downforce performance, but will also introduce additional complexity to the vehicle's flow field, affecting its pressure distribution and wake characteristics[28,29,35,20,14,8,5]. Additionally, based on the high sensitivity of isolated aerodynamic elements to dynamic operating conditions[16,9], high-performance vehicles are expected to exhibit a substantially elevated yaw sensitivity over passenger vehicles.

The additional flow field complexity of high-performance vehicles compared to automotive vehicles is also evident from studies on their straight-line wake characteristics. Passenger vehicles typically demonstrated a wake dominated by a counter-rotating vortex pair, formed behind the vehicle's base[31,21,44]. This vortex pair was inboard rotating for fastback and notchback vehicle types, and created a minor inboard downwash and outboard outwash effect. Vehicles with squared rear end geometries like estates and sport utility vehicles (SUV) depicted an outboard rotating vortex pair, which created a small inboard upwash and outboard inwash effect. Additionally, wake characteristics were found to be receptive to the complexity of the upper body design and the flow rate underneath the vehicle[34,17].

High-performance and racing vehicles on the other hand generally showed a wake dominated by vortical flow from aerodynamic devices on the upper surface like rear wings or spoilers, and strong upward flow components from the diffuser[40,43,27,13,31]. The combined effect of these aerodynamic devices resulted in a highly turbulent wake with a strong inboard upwash and outboard inwash effect.

In summary, the available literature has shown the substantial impact of yaw conditions on the aerodynamic performance and flow field of automotive vehicles. However, the effects of yaw conditions on the significantly more complex flow field of high-performance vehicles has not been adequately studied yet. The present study therefore investigates the specific effects of yaw conditions on the aerodynamic performance and flow field of various configurations of a high-performance vehicle reference model.

The analyses in this paper are based on experimental data of aerodynamic forces, surface pressures and wake total pressures from wind tunnel measurements in the 8x6 wind tunnel at Cranfield University. In addition, a complementary set of numerical results from Reynolds-Averaged Navier-Stokes (URANS) based computational fluid dynamics (CFD) simulations is provided to support the interpretation of the experimental data and facilitate a more comprehensive discussion on the effects of yaw conditions on the aerodynamic performance and flow field of high-performance vehicles.

2. Methodology

2.1. Vehicle Model

The DrivAer Fastback model[11] is a widely used generic vehicle model for aerodynamic research for automotive applications. The present study uses three configurations of a high-performance variant of this vehicle model, called the *DrivAer hp-F* model[32], which serves as a reference model for aerodynamic research for high-performance applications. The base of this vehicle model consists of a 35% scale DrivAer Fastback model with a smooth underbody, side mirrors, and stationary wheels.

The standard configuration of the *DrivAer hp-F* model is equipped with add-on devices including a 41 mm front bumper splitter, forebody strakes and a 10° underbody multichannel diffuser (Figure 1a). The spoiler configuration of the *DrivAer hp-F* model is equipped with an additional 350 mm x 80 mm spoiler at a 40° angle of attack (Figure 1b). The rear wing configuration of the *DrivAer hp-F* model is fitted with a NACA 6412 profile rear wing at a 15° angle of attack, which has a span of 420 mm and a chord length of 110 mm (Figure 1b). The parametric dimensions of the vehicle model are listed in Table 1, where the reference area corresponds to the configuration with rear wing.

Table 1: Parametric dimensions of the *DrivAer hp-F* model

Parameter	Value	Unit
Car scale (CS)	35	%
Length (L)	1.6144	m
Width (W)	0.6273	m
Height (H)	0.4890	m
Ride height (h_o)	0.0455	m
Area (A_{ref})	0.2647	m^2

2.2. Wind Tunnel Experiments

2.2.1. Cranfield University 8x6 Wind Tunnel

The wind tunnel campaign is conducted in the closed return 8x6 Wind Tunnel at Cranfield University. The standard test section is transformed using a 42 mm elevated floor, two-stage boundary layer suction system and rotating floor turntable, providing a 2.44 m by 1.79 m transformed test section. The first boundary layer suction system (BL1) consists of a scoop intake and is positioned 1.6 m upstream of the turntable. The second boundary layer suction system (BL2) operates by suction through a porous plate which is located 0.85 m upstream of the turntable. The experiments were subject to a blockage ratio of approximately 6.3% with the vehicle at 0° yaw.

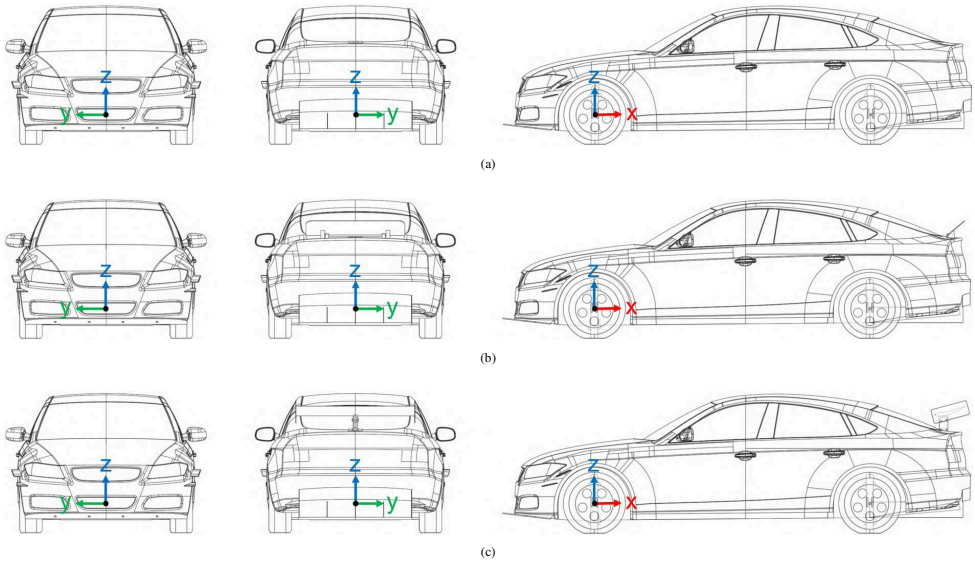

Figure 1: The *DrivAer hp-F* vehicle model configurations: (a) standard, (b) spoiler and (c) rear wing

2.2.2. Aerodynamic Forces

The aerodynamic forces of the three high-performance vehicle configurations are measured across a yaw angle range of -20° to 20° with increments of 5° and a wind speed of 40m/s. The aerodynamic force measurements are conducted using four independent six degree-of-freedom JR3 load cells, each positioned underneath a wheel of the vehicle model. The sensors have a nominal accuracy of ±0.25% of the full scale measuring range, which corresponds to a measurement accuracy for each sensor of ±1.11 N for drag and side force, and ±2.22 N for lift force.

Figure 2: 8x6 Wind Tunnel at Cranfield University

Data acquisition is performed by sampling at 1 kHz over a 20 s time interval for each yaw angle. A constant fan rotor speed throughout each yaw angle sweep provided a wind speed with a variance of ±0.1 m/s across each acquisition interval, and dropped with less than 0.6 m/s between straight-line and maximum yaw angles of ±20° due to increase blockage. Time-averaged quantities for the channels are created and converted into lift, drag, and side force coefficients using Eq.1. Here, F_i [N] is the measured force and C_i [-] is the non-dimensional coefficient with i used to indicate lift (L), drag (D) and side (S) forces. P_{dyn} [Pa] is the measured dynamic pressure in the freestream in the tunnel, and A_{ref} [m^2] is the reference area listed in Table 1.

$$C_i = \frac{F_i}{P_{dyn} \cdot A_{ref}} \tag{1}$$

The reliability of the aerodynamic force data is assessed by the repeatability between three complete yaw angle sweeps using the vehicle with rear wing configuration. The test-to-test repeatability is expressed for lift, drag, and side force coefficients by using the maximum absolute difference between the mean force coefficient at each yaw angle and the individual measurement points of the three repeated experiments at the corresponding yaw angles (Figure 3). The average of this maximum absolute deviation across the yaw angle range is $|\Delta C_L| \approx 0.0051$, $|\Delta C_D| \approx 0.0018$ and $|\Delta C_S| \approx 0.0062$ for the lift, drag and side

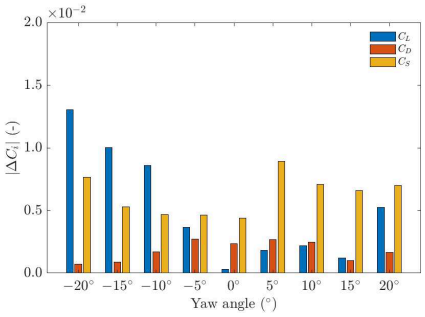

Figure 3: Repeatability of the aerodynamic force measurements on the vehicle with rear wing configuration across the yaw angle range

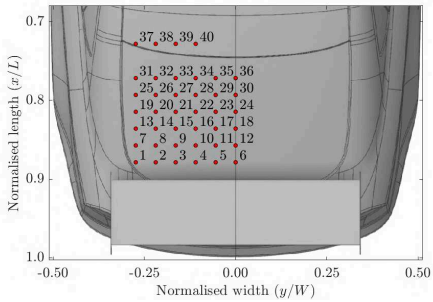

Figure 4: Surface pressure tap locations

force coefficients respectively.

2.2.3. Surface Pressure

Similarly to the aerodynamic force measurements, the surface pressure distributions along the slant of the three high-performance vehicle configurations are measured across the yaw angle range of -20° to 20° with increments of 5° and a wind speed of 40 m/s. The surface pressure measurements also used a constant fan rotor speed throughout the yaw angle sweeps, providing a comparable wind speed consistency to the aerodynamic force measurements.

The pressure distributions are obtained through 40 surface pressure taps, which are connected to two 20-channels differential pressure transducers that share an atmospheric reference pressure. The surface pressure data is sampled at 5 kHz over a 30 s time interval at each yaw angle. The time-averaged data is converted into pressure coefficients using Eq.2. Here, C_p (-) is the non-dimensional pressure coefficient, P_s (Pa) the measured pressure at the surface pressure taps, and P_{ref} (Pa) the atmospheric reference pressure measured outside the wind tunnel.

$$C_p = \frac{P_s - P_{ref}}{P_{dyn} \cdot A_{ref}} \tag{2}$$

To achieve high resolution surface pressure maps with the available channels, the surface pressure taps are positioned on one half of the slant (Figure 4). By testing both positive and negative yaw angles, the surface pressure data of an opposite yaw angle measurement can be transposed onto the side of the slant without surface pressure taps, using the surface taps along the symmetry line of the vehicle as overlapping data points. This combined data is interpolated using the spline method in MATLAB to create complete pressure maps across the full width of the slant.

The test-to-test repeatability of the surface pressure measurements is assessed based on three repeated yaw sweep experiments using the vehicle with rear wing configuration. Figure 5 shows the maximum absolute difference between a single measurement point and the mean pressure coefficient across the three repeated runs for each surface pressure tap at each yaw angle. Here, all measured surface pressure data is confined within a tolerance band of $|\Delta C_p| \approx 0.008$ with no outliers.

2.2.4. Wake Total Pressure

Total pressure measurements are conducted in the wake of the high-performance vehicle with rear wing configuration at a yaw angle range of -20° to 0° with increments of 5° and a wind speed of 40 m/s. The vehicle's wake at each yaw angle is measured across a width of 1200 mm (1.91W) at three planes defined as P1, P2 and P3 which are positioned at 400 mm (0.25L), 700 mm (0.43L) and 1000 mm (0.62L) downstream of the vehicle respectively (Figure 6).

The measurements are conducted with a pressure rake consisting of 39 vertically stacked single hole probes which can be positioned by an automated traverse system. The pressure rake is connected to two 20-channels differential pressure transducers that share an atmospheric reference pressure. The probes in the pressure rake have a nominal vertical spacing of 4.77 mm, which cover a total height of 181.26 mm. A cost-effective horizontal resolution of 25 mm is used[31], resulting in 49 horizontal steps per horizontal sweep. To capture the entire wake height,

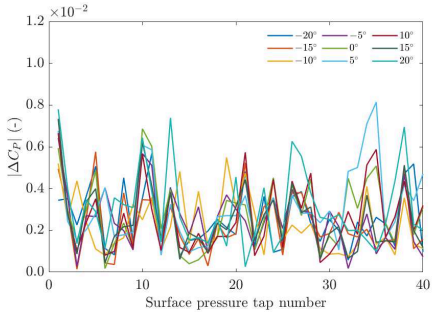

Figure 5: Repeatability of the surface pressure measurements on the vehicle with rear wing configuration across the yaw angle range

Figure 6: Wake total pressure measurements setup

four horizontal sweeps are stacked, using at a minimum of 5 overlapping probes between each vertical stack. The ground clearance of the first vertical stack varies between 5 mm and 15 mm across the wake planes due to imperfections in the wind tunnel flooring system.

The data at each position is acquired at 1 kHz over a 10 s time interval. The time-averaged total pressure data is converted into total pressure coefficients using Eq.3. Here, C_{pT} (-) is the non-dimensional total pressure coefficient and P_{t} (Pa) the measured pressure at probes in the wake.

$$C_{\mathrm{pT}} = \frac{P_{\mathrm{t}} - P_{\mathrm{ref}}}{P_{\mathrm{dyn}} \cdot A_{\mathrm{ref}}} \tag{3}$$

Complete total pressure maps of the wake are created by interpolating the time-averaged data in MATLAB, where averaged quantities of overlapping probes from subsequent vertical stacks are used. Contrary to the other experiments, the fan rotor speed could be adjusted after each horizontal sweep. This provided a wind speed with fluctuations within ±0.1 m/s across each acquisition interval and a variance restricted to ±0.2 m/s across the yaw angle range.

Due to the significant duration of the measurement of one complete wake plane, the repeatability of the wake total pressure measurements is assessed based on three repeated horizontal sweeps at the same vertical position. The repeated experiments are conducted on the second vertical stack of P3 with the vehicle at 0° of yaw. The second vertical stack is located in a highly turbulent region of the wake and should therefore provide a worst-case representation of the repeatability of the complete wake plane measurements. Figure 7 depicts the maximum absolute differences between a single measurement point and the mean total pressure coefficients across the three repeated runs. All observed pressure differences are within a tolerance band of $|\Delta C_{\mathrm{pT}}| \approx 0.017$ whereby 90% of the data varies by less than $|\Delta C_{\mathrm{pT}}| \approx 0.0065$.

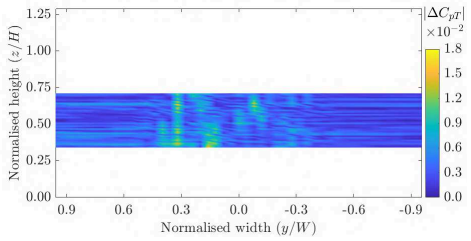

Figure 7: Repeatability of the wake total pressure measurements on the second vertical stack of the P3 plane behind the high-performance vehicle with rear wing configuration at 0° yaw

2.3. Numerical Simulations

2.3.1. Computational Domain & Boundary Conditions

The computational domain is designed as a straight tunnel, which matches the dimensions of the test section of the 8x6 Wind Tunnel at Cranfield University (Figure 8). To provide sufficient space for turbulent characteristics and wake development, the velocity inlet is positioned 3L in front and the pressure outlet 5L behind the vehicle model[18], resulting in a total domain length of 14904 mm.

The simplified BL2 system extends across the full width of the tunnel, and the wind tunnel floor upstream of this system is modelled as a symmetry wall to prevent boundary layer growth. The wind tunnel floor downstream of the BL2 system and the remaining wind tunnel walls are modelled as no-slip stationary walls. The simulations are performed on the high-performance vehicle with rear wing configuration across a yaw angle range of 0° to 20° with increments of 5°. Operating conditions which resemble the varying wind tunnel conditions are listed in Table 2 and applied for improved correlation.

2.3.2. Mesh

ANSYS Fluent Meshing software is used to create unstructured poly-hexcore meshes for the yaw simulations. Increased numerical workflow efficiency is achieved by the creation of separate domains for the vehicle model and wind tunnel, which allows yaw angle rotation without re-meshing. This approach allows a cylindrical volume mesh including the vehicle model to be connected to the wind tunnel volume mesh at any yaw angle through a mesh interface (Figure 9). Variation in lift and

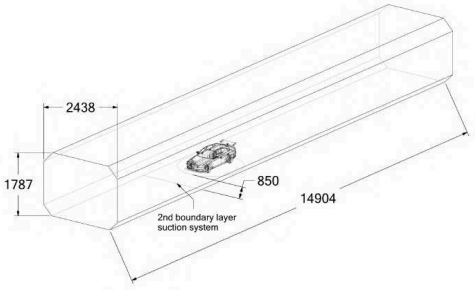

Figure 8: Computational domain with dimensions in mm

Table 2: Reference operating conditions for yaw simulations

Parameter	0° Yaw	-5° Yaw	-10° Yaw	-15° Yaw	-20° Yaw	Unit
Temperature (T_{ref})	30	30	30	30	30	°C
Velocity (U_{ref})	40.00	39.93	39.75	39.60	39.42	m/s
Dynamic Pressure ($P_{\text{d,ref}}$)	917.30	913.80	906.01	898.32	889.94	Pa
Density (ρ_{ref})	1.1472	1.1464	1.1468	1.1457	1.1454	kg/m^3
Dynamic Viscosity (μ_{ref})	18.616e-6	18.616e-6	18.616e-6	18.616e-6	18.616e-6	kg/m s
Turbulent Intensity (I_{ref})	0.052	0.052	0.052	0.052	0.052	%

drag coefficients with a conventional singular domain meshing approach is approximately 0.1%, implying the accuracy of the simulations is unaffected.

The element sizes and near-wall treatments used in this study are based on a previously extensively validated mesh strategy for cost-effective aerodynamic simulations on high-performance vehicles[29]. The base element size and vehicle surface element size are approximately 7.25% and 0.45% of the vehicle's length, respectively. Vehicle surface element sizes are reduced to about 2.5% of the vehicle's length on aerodynamic devices, and to 0.25% on small geometric features. Medium near-wall treatments with a $y^+ \approx$ 120-150 and about 4-6 inflations layers are used on the vehicle and wind tunnel walls to capture their boundary layers. Additionally, four refinement zones with gradually increasing element sizes are used to effectively capture the vehicle's near-field and wake region in more detail (Figure 9). Overall, the mesh contains nearly 13.6 million cells.

2.3.3. Turbulence Model

This study solves the unsteady, isothermal, and incompressible Navier-Stokes equations without source terms using the k-ω SST turbulence model[24] in ANSYS Fluent. This model is chosen for its proven balance between accuracy and computational costs in a previous study with the same geometry and flow domain[29].

The continuity and momentum equations are expressed by Eq.(4) and Eq.(5), where $\mathbf{u}$ (m/s) and p (Pa) denote the mean velocity and pressure, respectively.

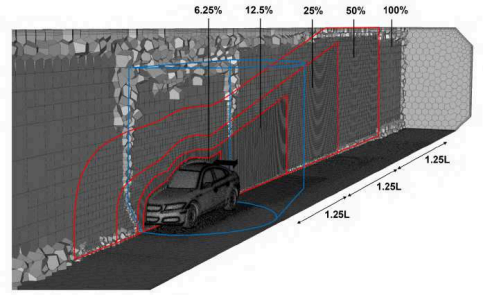

Figure 9: Volume mesh slice at $y = 0$ (symmetry) with highlighted mesh interface in blue and refinement zones in red

$$\nabla \cdot \mathbf{u} = 0 \tag{4}$$

$$\frac{\partial \mathbf{u}}{\partial t} + (\mathbf{u} \cdot \nabla)\mathbf{u} = \frac{1}{\rho}\nabla p + \nabla \tau \tag{5}$$

Stresses in the fluid are represented by τ (Pa). Using Boussinesq's linear eddy viscosity assumption, the stress tensor τ is expressed by Eq.(6).

$$\tau = 2\nu_t \mathbf{S} - \frac{2}{3}(\nabla \cdot \mathbf{u}) \cdot \mathbf{I} \tag{6}$$

The turbulent viscosity is denoted by ν_t (m^2/s), which is obtained by the k-ω SST turbulence model. $\mathbf{I}$ represents the identity matrix and $\mathbf{S}$ signifies the strain rate tensor, expressed by Eq.(7).

$$\mathbf{S} = \frac{1}{2}[(\nabla \mathbf{u}) + (\nabla \mathbf{u})^T] \tag{7}$$

The k-ω SST turbulence model is solved in its classical form[24], where the transport equations for the turbulent kinetic energy k (m^2/s^2) and the specific dissipation rate ω (s^{-1}) are given by Eq.(8) and Eq.(9), respectively. The generation (G), diffusivity (Γ), dissipation (Y), cross-diffusion (D) and source terms (S) are expressed following ANSYS Fluent's formulation[2].

$$\frac{\partial k}{\partial t} + \mathbf{u} \cdot \nabla k = \Gamma_k \nabla^2 k + G_k - Y_k + S_k \tag{8}$$

$$\frac{\partial \omega}{\partial t} + \mathbf{u} \cdot \nabla \omega = \Gamma_\omega \nabla^2 \omega + G_\omega - Y_\omega + D_\omega + S_\omega \tag{9}$$

The turbulent viscosity ν_t is subsequently computed from the turbulent kinetic energy k and the specific dissipation rate ω, as expressed by Eq.(10)

$$\nu_T = \frac{k}{\omega} \tag{10}$$

Pressure-velocity coupling is performed using the coupled scheme. The momentum and transport equations are spatially discretised using the second-order upwind scheme, and temporally discretised using the bounded second-order implicit scheme.

Following established guidelines[29], each yaw angle simulation was executed with a fixed time-step of $3.125 \cdot 10^{-4}$ s and a maximum of 20 inner iterations over a total flow time of 1.2 s, equivalent to 29.7 convective time units. Statistical convergence was reached within the first 0.6 s, after which averaged quantities and unsteady statistics were collected over the remaining 0.6 s of flow time. The simulations were carried out on

eight AMD EPYC 7543 CPUs using a total of 256 cores, which resulted in an average computational time of approximately 50 hours per yaw angle simulation.

3. Validation

This section validates the results from the complementary numerical simulations against experimental measurement data. The aim of the supplementary numerical results is to support the interpretation of the experimental data presented in this paper and provide a more comprehensive discussion on the effect of yaw conditions on high-performance vehicle aerodynamics. The numerical results should therefore be able to capture the relative effects of yaw conditions on the vehicle's aerodynamic performance and associated dominant flow features.

Some variation between the experimental and numerical results is anticipated due to limitations in the computational representation of the experimental setup and inherent challenges in the prediction of wind tunnel conditions[1]. The standard atmospheric operating pressure from the numerical results is therefore matched to the measured operating pressure from the wind tunnel experiments by an approximate $\Delta C_p \approx -0.25$ correction to support direct trend comparisons in this section.

3.1. Aerodynamic Forces

Figures 10, 11 and 12 illustrate the experimental and numerical results of total lift, drag, and side force coefficients, with additional representations of the force contributions from the rear wing. The numerical results in Figure 10 demonstrate an overprediction in straight-line total downforce of $\Delta C_L \approx -0.15$, and depict only 30% of the lift increase across the yaw angle range. The higher yaw sensitivity observed in the experimental data can be explained by a reduced airflow momentum underneath the vehicle, caused by turntable surface imperfections and unevenness between the wind tunnel floor and turntable system. These subtle wind tunnel floor details are practically not feasible to recreate in the computational wind tunnel, and consequently cause the simulations to predict a stronger underbody downforce generation. This hypothesis is further supported by the remarkably good correlation of the rear wing's downforce contribution, which demonstrates a comparable yaw sensitivity and an average deviation of only $\Delta C_L \approx 0.02$ between the experimental and numerical results.

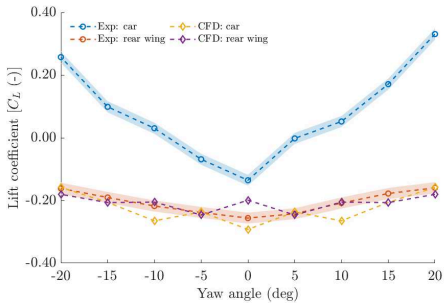

Figure 10: Experimental and numerical results of lift coefficients on the high-performance vehicle with rear wing configuration, including force contributions from the rear wing. Shaded bars indicate the accuracy of measurement data.

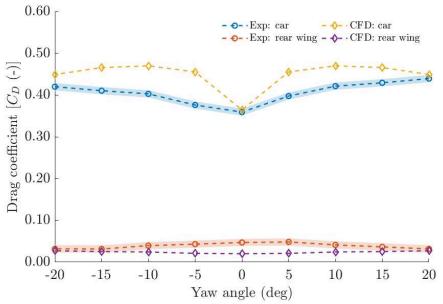

Figure 11: Experimental and numerical results of drag coefficients on the high-performance vehicle with rear wing configuration, including force contributions from the rear wing. Shaded bars indicate the accuracy of measurement data.

Figure 11 reveals that the overprediction in total downforce also contributes to about $\Delta C_D \approx 0.04$ more drag for the numerical results across the yaw angle range. Similarly to downforce, improved correlation on the rear wing's drag contribution is observed. Both the experimental and numerical results demonstrate that the drag coefficient is relatively invariant to the yaw conditions, with an average deviation of $\Delta C_D \approx 0.02$.

The experimental and numerical results of side force coefficients in Figure 12 show a comparable yaw sensitivity across the yaw angle range, but the numerical results generally overpredict total side force by $\Delta C_S \approx 0.12$. The prediction of side forces generated by the rear wing demonstrates an improved correlation, with only an average deviation of $\Delta C_S \approx 0.03$ to

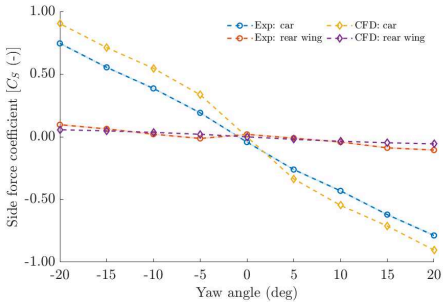

Figure 12: Experimental and numerical results of side force coefficients on the high-performance vehicle with rear wing configuration, including force contributions from the rear wing. Shaded bars indicate the accuracy of measurement data.

the experimental data across the yaw angle range.

3.2. Surface Pressure

Figure 13 shows the experimental and numerical results of surface pressure coefficients on the slant of the high-performance vehicle with rear wing configuration. The simulations predict a slightly more gradual pressure recovery, especially at yaw angles of <15°. Yet, the general effect of yaw conditions are adequately captured, shown by the qualitative agreement of the leeward shift of the pressure recovery and the emerging low pressure region from the top windward corner of the slant.

3.3. Wake Total Pressure

The experimental and numerical results of total pressure coefficients on the P1 plane behind the high-performance vehicle with rear wing configuration are presented in Figure 14. The numerical results generally show less pressure losses outside the main wake at y/W < -0.4 at larger yaw angles due to the simplified BL2 system (section 2.3.1). Discrepancies in pressure losses in the lower wake region, which is dominated by airflow from underneath the vehicle, are also observed. This finding supports the hypothesis that the underbody airflow is a main source of discrepancy between the experimental and numerical results.

Nonetheless, the predictions of relative total pressure magnitudes show good correlation with the experimental data. Moreover, dominant flow features like the diffuser upwash at $y/W \approx 0$, $z/H \approx 0.3$, and the counter-rotating vortex pair from the rear wing at $y/W \approx \pm 0.28$, $z/H \approx 0.83$ are adequately captured at 0° yaw. The numerical results also show good qualitative agreement with the experimental results on the formation of the strong vehicle body vortex, represented by the low total pressure trace at $z/H \approx 0.75$, and its impact on the general wake structure across the yaw angle range.

3.4. Summary

The validation results show satisfactory agreement with experimental results of aerodynamic forces from the rear wing, and more detailed surface pressure data on the slant and total pressure data in the wake. The results of total force coefficients are affected by underbody airflow momentum discrepancies resulting from wind tunnel floor details. Overall, the validation results provide confidence in the accuracy of the numerical results and will therefore be used complementary to the experimental data to formulate a more comprehensive understanding of the effects of yaw conditions on the aerodynamic performance and flow field of high-performance vehicles.

4. Results & Discussions

Experimental measurement results of aerodynamic forces on the standard, spoiler, and rear wing configurations of the *DrivAer hp-F* model are presented in section 4.1 and used to investigate the effects of yaw conditions on the overall aerodynamic performance of these configurations. Before the investigation of more detailed data, numerical representations of the flow field of the *DrivAer hp-F* model with rear wing configuration are provided in section 4.2 to illustrate the general effects of yaw conditions on the vehicle's flow field. Subsequent, experimental and numerical results of surface pressure coefficients are discussed in section 4.3 to analyse the effects of yaw conditions on the pressure distribution on the vehicle. Lastly, experimental measurement results of total pressure coefficients in the wake of the *DrivAer hp-F* model with rear wing configuration are presented in section 4.4 to discuss the effects of yaw conditions on the wake characteristics and dominant structures. Throughout the presented results, positive yaw angles correspond with a counter-clockwise rotation of the vehicle model.

4.1. Aerodynamic Forces

This section presents experimental measurement results of lift, drag, and side force coefficients on the standard, spoiler, and rear wing configurations of the *DrivAer hp-F* model. The results are illustrated across both positive and negative yaw angles. This implies that the right side of the vehicle is the windward side at positive yaw angles, but becomes the leeward side at negative yaw angles. Minor asymmetry is observed across the presented experimental data, which indicates that physical limitations are present in the load cells alignment, flow alignment and symmetry of the vehicle model. However, the asymmetric effects manifest as relatively small systematic offsets in the force measurements and therefore do not hinder the analysis of the vehicle's yaw sensitivity.

4.1.1. Lift Coefficients

The lift coefficients illustrated in Figure 15 reveal that the standard configuration reaches a minimum total lift coefficient of $C_L \approx 0.12$ at 0° yaw. In this condition, the vehicle has a lift coefficient of $C_L \approx -0.04$ at the front axle, and $C_L \approx 0.16$ at the rear axle. This lift force distribution implies that front body aerodynamic devices like the splitter and strakes, combined with initial airflow acceleration underneath the vehicle, promote minor downforce generation at the front axle. Contrarily, rear axle downforce generation is anticipated to be hindered by the absence of a moving ground in the yaw experiments. Moreover, the additional reduction in airflow momentum caused by surface imperfections and unevenness along the wind tunnel floor is expected to further reduce the full downforce potential of the vehicle's underbody and diffuser seen in previous work [28].

Additionally, the standard configuration start to generate substantially more lift at larger yaw angles, reaching an average maximum total lift coefficient of $C_L \approx 0.45$ at ±20° yaw. The downforce generation on the leeward front wheel increases initially by $\Delta C_L \approx -0.02$ and remains somewhat constant beyond

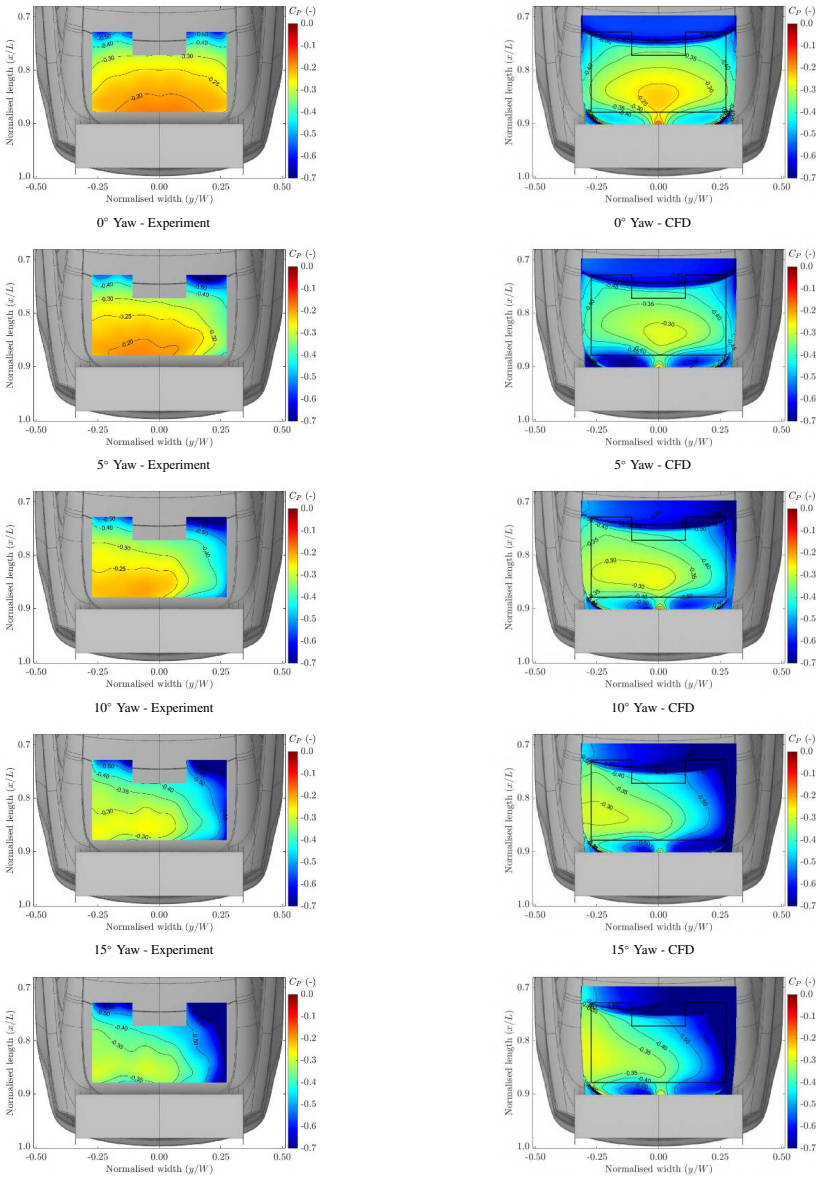

Figure 13: Experimental and numerical results of time-averaged surface pressure coefficients C_p on the slant of the high-performance vehicle with rear wing configuration across the yaw angle range

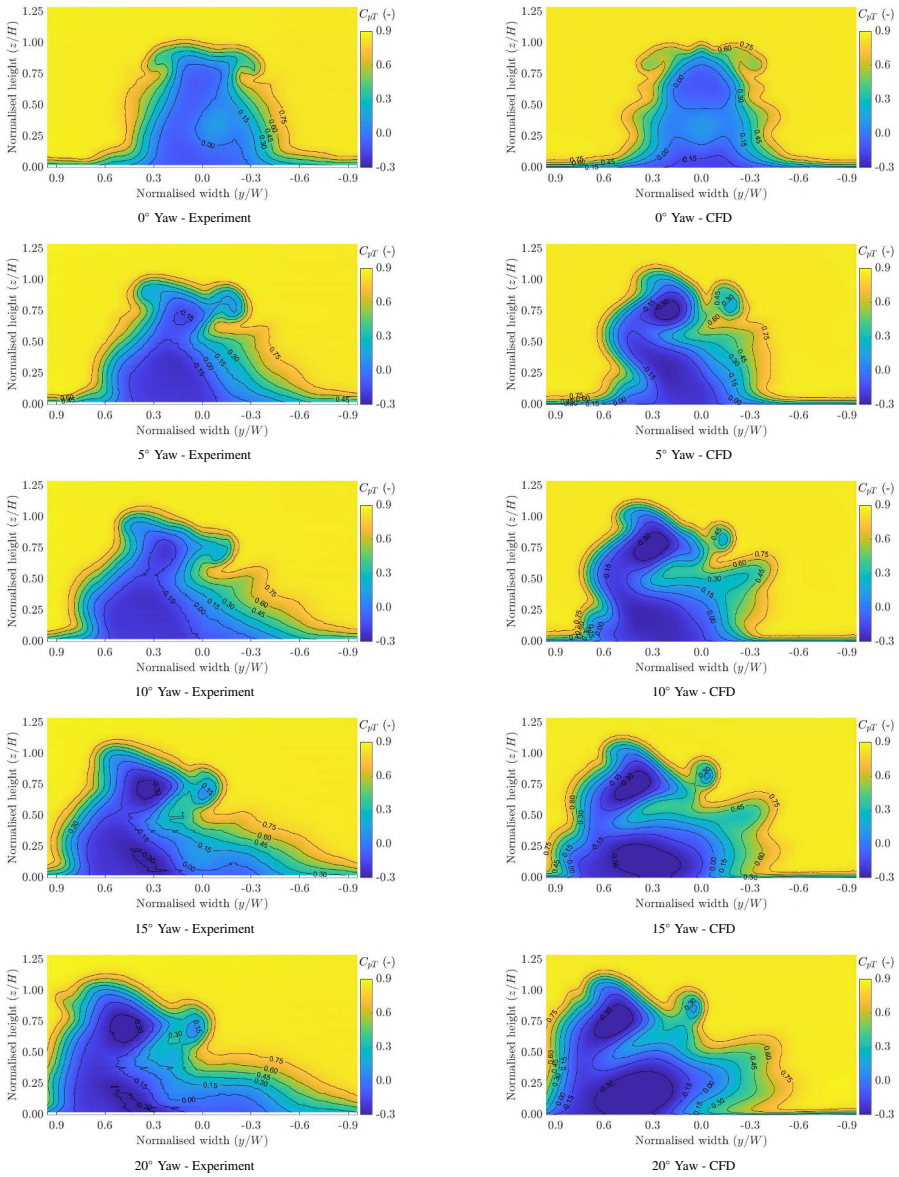

Figure 14: Experimental and numerical results of time-averaged total pressure coefficients C_{pT} on the P1 wake plane of the high-performance vehicle with rear wing configuration across the yaw angle range

±5° yaw. The lift generation on the leeward rear wheel also reduces, but with more gradual decrements of $\Delta C_L \approx -0.01$ at each yaw angle up to ±15°. Contrarily, the lift coefficient on the windward front wheel increases with increments of $\Delta C_L \approx 0.05$ at each yaw angle. The lift generation on the windward rear wheel increases by $\Delta C_L \approx 0.07$ at 5° yaw, but levels off to increments of $\Delta C_L \approx 0.02$ at larger yaw angles.

The spoiler configuration reaches a minimum total lift coefficient of $C_L \approx -0.05$ at 0° yaw and thereby generates downforce. In this straight-line condition, the addition of the spoiler has increased rear axle downforce by $\Delta C_L \approx -0.19$, but increased front axle lift by $\Delta C_L \approx 0.02$, leading to a maximum total downforce gain of $\Delta C_L \approx -0.17$. The relative influence of the spoiler on each individual wheel remains relatively constant throughout the yaw angle range, except for the windward rear wheel. The diminishing relative offset in lift coefficients on the windward rear wheel between the spoiler and standard configuration indicates that the windward side of the spoiler loses downforce at larger yaw angles. The yaw sensitivity of the spoiler is also evident from the total lift coefficient trend, where the spoiler configuration experiences a $\Delta C_L \approx 0.41$ increase in lift between 0° yaw and ±20° yaw, which is approximately 23% higher than for the standard configuration.

The rear wing configuration provides most downforce across the yaw angle range and reaches a minimum total lift coefficient $C_L \approx -0.14$ at 0° yaw. The total downforce generation in straight-line conditions has therefore been improved by $\Delta C_L \approx -0.26$ over the standard configuration, which is approximately 50% more additional downforce than provided by the spoiler. The influence of the rear wing is attributed to a $\Delta C_L \approx -0.32$ increase in rear axle downforce and a $\Delta C_L \approx 0.06$ increment in front axle lift at 0° yaw. Contrary to the other configurations, the dominant rearward shift of the downforce distribution has resulted in a minor total lift generation on the front axle. In addition, the lift coefficients on the windward rear wheel from the rear wing depict again a diminishing relative offset to results from the standard configuration at larger yaw angles. This yaw sensitivity is also apparent from the total lift coefficient trend, where the rear wing configuration experiences a lift increase of $\Delta C_L \approx 0.43$ between 0° yaw and ±20° yaw, which is approximately 29% more than the standard configuration and 5% more than the spoiler configuration. Section 4.3.3 will discuss that the high yaw sensitivity from the rear wing configuration is explained by downforce losses resulting from substantial flow obstruction from the windward endplate.

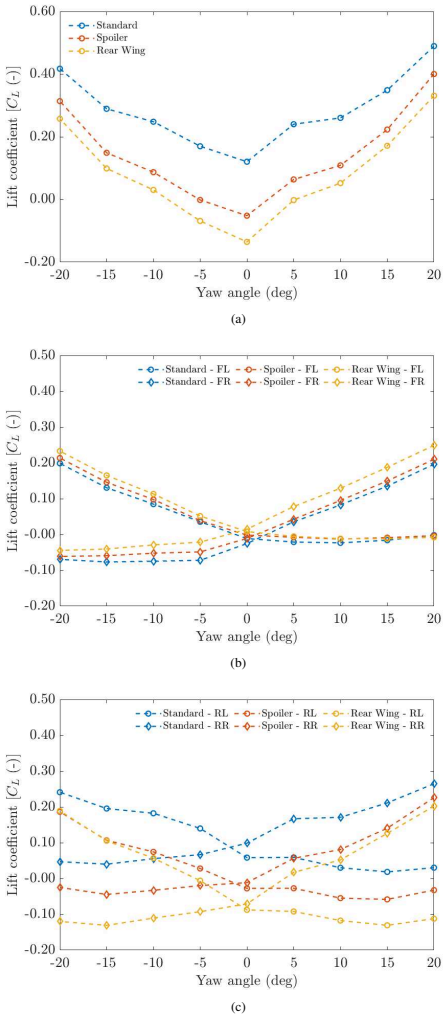

Figure 15: Experimental data of (a) total lift, (b) front axle lift, and (c) rear axle lift coefficients on the standard, spoiler, and rear wing high-performance vehicle configurations across the yaw angle range

4.1.2. Drag Coefficients

Figure 16 demonstrates that yaw conditions have a strong non-linear effect on the drag coefficients of each configuration, where the magnitude of a subsequent drag increment reduces at larger yaw angles. The standard configuration reaches a minimum drag coefficient of $C_D \approx 0.31$ at 0° yaw, resulting in a maximum aerodynamic efficiency of $-C_L/C_D \approx -0.39$. The standard configuration only achieves negative aerodynamic efficiencies, since it does not generate downforce at any yaw angle. The drag coefficient reaches a maximum of $C_D \approx 0.40$ at ±20° yaw, where a minimum aerodynamic efficiency of $-C_L/C_D \approx -1.14$ is achieved.

The spoiler configuration produces a minimum drag coefficient of $C_D \approx 0.35$ at 0° yaw, which is approximately 12% higher than the standard configuration. The maximum drag coefficient of $C_D \approx 0.41$ is reached at ±20° yaw, which is only 3% higher than the standard configuration. So, the initial drag

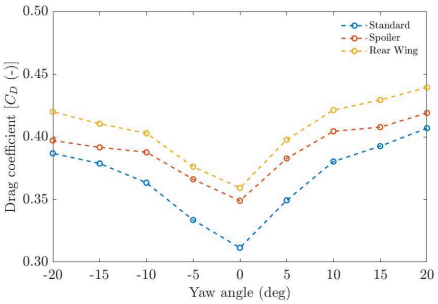

Figure 16: Experimental data of drag coefficients on the standard, spoiler, and rear wing high-performance vehicle configurations across the yaw angle range

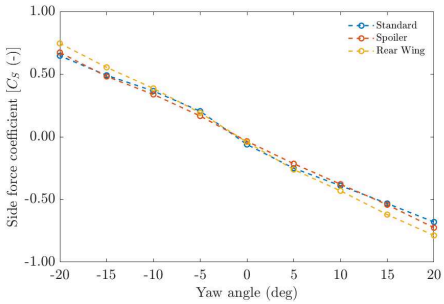

Figure 17: Experimental data of side force coefficients on the standard, spoiler, and rear wing high-performance vehicle configurations across the yaw angle range

increment of $\Delta C_D \approx 0.04$ at 0° yaw is reduced to $\Delta C_D \approx 0.01$ at ±20° yaw, indicating that the additional drag produced by the spoiler reduces at larger yaw angles. This finding is in accordance with the yaw sensitivity observed for the lift coefficients, where a reduction in pressure build-up at the windward side of the spoiler at larger yaw angles reduces its contribution to both downforce and drag. Overall, the spoiler configuration reaches a maximum aerodynamic efficiency of $-C_L/C_D \approx 0.15$ at 0° yaw and a minimum of $-C_L/C_D \approx -0.87$ at ±20° yaw.

The rear wing configuration reaches a minimum drag coefficient of $C_D \approx 0.36$ at 0° yaw, which is approximately 15% higher than the standard configuration and 3% higher than the spoiler configuration. The maximum drag coefficient of $C_D \approx 0.43$ is produced at ±20° yaw, which is only 8% higher than the standard configuration but 5% higher than the spoiler configuration. The diminishing drag increment relative to the standard configuration indicates that the additional drag produced by the rear wing also reduces at larger yaw angles. However, the relative drag increment from the spoiler configuration to the standard configuration diminishes quicker, implying a higher yaw sensitivity. Despite the high drag coefficients, the rear wing configuration reaches a maximum aerodynamic efficiency of $-C_L/C_D \approx 0.38$ at 0° yaw, which is more than double the efficiency of the spoiler. The minimum aerodynamic efficiency of $-C_L/C_D \approx -0.68$ is reached at ±20° yaw, which is still approximately 20% higher than the spoiler configuration.

4.1.3. Side Force Coefficients

The sides force coefficients from each configuration, illustrated in Figure 17, increase fairly linearly across the yaw angle range. Section 4.3.1 will show that this is a result of an increasing high pressure region on the windward side of the vehicle. The standard configuration reaches a maximum side force coefficient of $C_S \approx \pm 0.66$ at ±20° yaw. The addition of the spoiler increases the maximum side force coefficient by about 5% to $C_S \approx \pm 0.70$ at ±20° yaw. The larger side profile from the rear wing results in the largest side force coefficient of $C_S \approx \pm 0.77$ at ±20° yaw, which is approximately 16% higher than the standard configuration and 10% higher than the spoiler configuration.

4.2. Flow Field

4.2.1. Wake Structures

Numerical representations of the wake structures on the *DrivAer hp-F* model with rear wing configuration are presented in Figure 18a. These results reveal that at 0° yaw, most severe flow separation occurs at the wheels and behind the vehicle's base. Smaller separated flow regions are also observed at the splitter, mirrors and rear wing. When the vehicle is subject to yaw conditions, the flow separation underneath the splitter shifts leeward and becomes less severe. The wake from the windward mirror diminishes across the yaw angle range, while the wake from the leeward mirror increases in size.

The wheel wakes generally increase in size and start to develop with the direction of the freestream airflow. Consequently, the windward wheel wakes propagate inboard and cause interference effect throughout the underbody and diffuser regions of the vehicle. The leeward wheel wakes propagate outboard and cause additional flow separation along the leeward side of the vehicle. In addition, the yaw conditions cause more flow separation at the rear wing's lower surface and support structure. Vortical flow generated at the rear wing also increases in strength and size across the yaw angle range. Finally, the vehicle's wake demonstrates the formation of a strong inboard rotating vortex at the windward side of the vehicle in yaw conditions. This vehicle body vortex increases in size and becomes the most prominent wake structure at larger yaw angles.

4.2.2. Turbulent Structures

Figure 18b presents numerical representations of the turbulent structures on the *DrivAer hp-F* model with rear wing configuration. The vehicle at 0° yaw depicts small streamwise vortices along the a-pillars. More distinct vortex structures are created at the rear wing, due to the pressure difference with the freestream airflow outboard of the endplates. The pressure difference with the rear wing's upper surface produces outboard rotating vortices, while the pressure difference with the rear

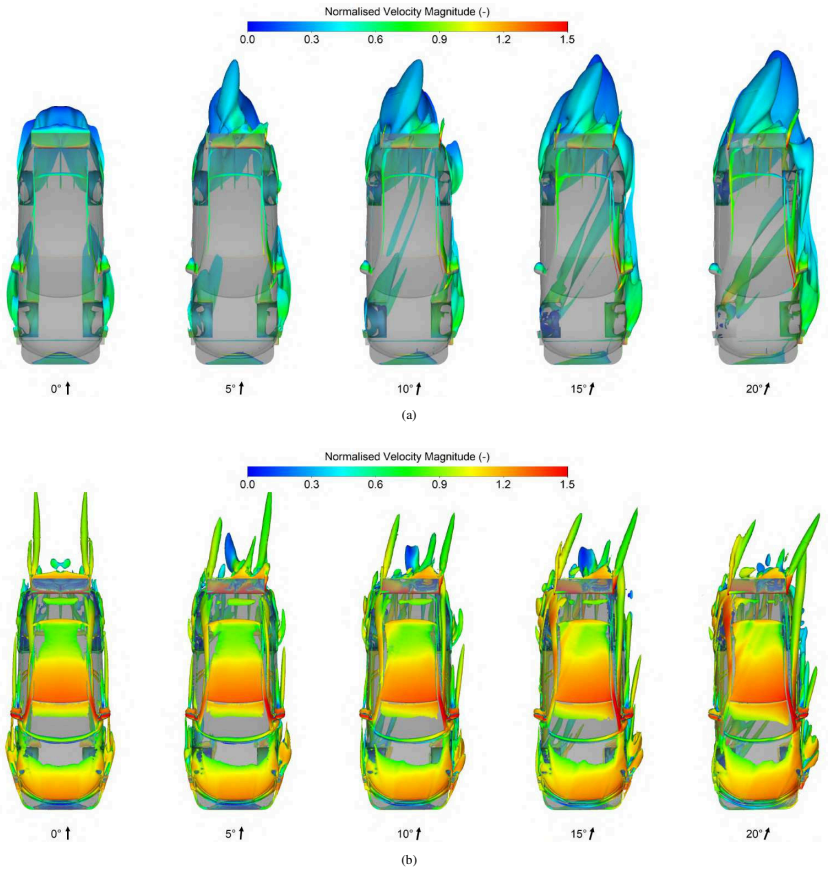

Figure 18: Numerical representations of the flow field of the high-performance vehicle with rear wing configuration through iso-surfaces of (a) zero total pressure and (b) q-criterion ($QL_\infty/U_\infty = 130$) coloured by normalised velocity magnitude across the yaw angle range

wing's lower surface produces inboard rotating vortices. The magnitude of the pressure difference with the rear wing's lower surface is more substantial and consequently produces a noticeably larger vortex.

The yaw conditions cause the windward a-pillar vortex to reduce in size, while the leeward a-pillar vortex significantly increases in size and starts to propagate further outboard. Section 4.3.3 will discuss that the yaw conditions cause an increasing pressure build-up on the outboard side of the windward endplate and on the inboard side of the leeward endplate. Consequently, Figure 18b shows that the formation of an outboard rotating vortex on the windward side of the rear wing's upper surface is suppressed and the formation of an inboard rotating vortex is even initiated here at larger yaw angles. The pressure build-up outboard of the windward endplate also promotes the formation of an inboard rotating vortex on the windward side of the rear wing's lower surface. Inversely, the formation of an outboard rotating vortex on the leeward side of the rear wing's upper surface is promoted, whereas the formation of an inboard rotating vortex on the leeward side of the rear wing's lower surface is suppressed.

4.3. Pressure Distribution

4.3.1. Vehicle Body

Numerical results of time-averaged surface pressure coefficients on the *DrivAer hp-F* model with rear wing configuration are presented in Figure 19. The vehicle exhibits generally a symmetric pressure distribution at 0° yaw. The front view reveals that the frontal impact of the airflow creates a stagnation zone at the nose, which is followed by a reduction in pressure as

the airflow accelerates around the curvature of the nose. The top view demonstrates a gradual pressure recovery along the bonnet towards the high pressure concentration at the windscreen. The airflow accelerates again around the curvature of the a-pillars and roof leading edge, creating low pressure regions. A slight rise in pressure along the roof is followed by a distinct pressure recovery zone on the slant, which develops towards the rear wing support.

Only one side view is presented at 0° yaw because of its symmetric averaged flow field. The side view depicts low pressure regions around the curvatures of the front wheel arch, a-pillar, roofline, and behind the rear wheel arch. A relatively constant low pressure is observed along the door panels and windows. The bottom view demonstrates a local low pressure concentration at the centre of the splitter, caused by flow separation at its sharp leading edge. A larger low pressure region is observed between the front wheels, due to initial airflow acceleration underneath the vehicle, which is followed by a slight pressure recovery along the floor. The diffuser depicts a low pressure region at the inlet, followed by a gradual pressure increase along the diffuser ramp. The back view generally displays a moderately low pressure across the base of the vehicle. Concentrations with lower pressures are observed on the top and bottom corners of the base, which are caused by the upper and lower airflow recirculation zones just behind the vehicle's base.

The significant influence of the yaw conditions on the pressure distribution are evident from the notable shift in pressure coefficients across the yaw angle range in Figure 19. The front views reveal that the yaw conditions move the stagnation zone at the nose towards the windward side. Larger low pressure regions are created on the leeward side of the nose and bonnet, due to additional airflow acceleration along their curvatures. Consequently, the local drag build-up at the nose is reduced by approximately 26% at 20° yaw compared to 0° yaw.

The top views demonstrate that the high pressure concentration on the windscreen is also moved towards the windward side in yaw conditions. Furthermore, stronger airflow acceleration on top of the vehicle increases the size of the low pressure regions on the roof and windward roofline. As a result, local lift generation on the roof has increased by approximately 19% at 20° yaw compared to 0° yaw. The airflow velocity along the windward c-pillar also rises with yaw angle, which creates an increasing low pressure region that spreads leeward onto the slant. The subsequent shift in pressure distribution along the slant and rear wing will be discussed in more detail in sections 4.3.2 and 4.3.3.

The bottom views show that an increasing high pressure concentration is created underneath the splitter, due to the changing impact angle of the airflow in yaw conditions. The flow separation at the splitter's leading edge and the associated low pressure concentration reduce in size and shift towards the leeward side. Furthermore, the effective inlet area to the front of the vehicle's underbody is reduced at larger yaw angles, which has a diminishing effect on the low pressure region between the front wheels. The reduction in effective inlet area is caused by the large flow obstruction from the windward front wheel in yaw conditions, which is evident from its increasing low pressure wheel wake. Despite the reduction in effective inlet area to the front of the underbody, airflow also enters the underbody from the windward side of the vehicle at larger yaw angles. This is indicated by the increasing size of the low pressure concentration at the windward edge of the underbody. In addition, the sidewards inlet of airflow to the underbody shifts the depression in pressure at the diffuser inlet towards the windward side. The angle between the airflow and the separators in the diffuser also creates vortices on the leeward side of the diffuser channels, indicated by the low pressure concentrations.

The side views demonstrate that the increasing low pressure regions along the leeward side of the nose and bonnet extend towards the leeward front wheel, while the pressure distribution along the leeward door panels remains relatively constant throughout the yaw angle range. Contrarily, the yaw conditions create an increasing high pressure region behind the windward front wheel and along the windward door panels. Figure 18b illustrated that the yaw conditions promote the formation of the leeward a-pillar vortex and suppress the formation of the windward a-pillar vortex, which is also apparent from the size of the low pressure concentrations in the respective areas. The pressure distributions along the leeward roofline and c-pillar seem to be affected by the trajectory of the strong leeward a-pillar vortex, and therefore only show a slight pressure rise at larger yaw angles. The windward roofline and c-pillar on the other hand depict a strong reduction in pressure across the yaw angle range due to additional airflow acceleration around these curvatures. The windward rear quarter panel also displays an increasing low pressure region, whereas the leeward rear quarter panel demonstrates a gradual pressure rise just behind the rear wheel. The leeward rear quarter panel only depicts an increasing low pressure concentration around the downstream edge, which is created by airflow that rolls-up into a recirculation zone close to the leeward side of the vehicle's base in yaw conditions.

The back view reveals a significant change in the pressure distribution along the vehicle's base. The modest pressure rise seen on the windward side of the vehicle's base is associated with the formation of a strong streamwise vortex at the windward side of the vehicle body, as previously identified in Figure 18a. This vehicle body vortex is generated by the inboard rotation of the above-mentioned high velocity airflow from the windward c-pillar and rear quarter panel. Lower velocity airflow along the leeward side of the slant and rear quarter panel flows around the periphery of the base and rolls-up into recirculation wake vortices. These recirculation wake vortices extend in the spanwise direction as they are drawn towards the dominant vehicle body vortex and consequently create the low pressure regions observed on the leeward side of the vehicle's base.

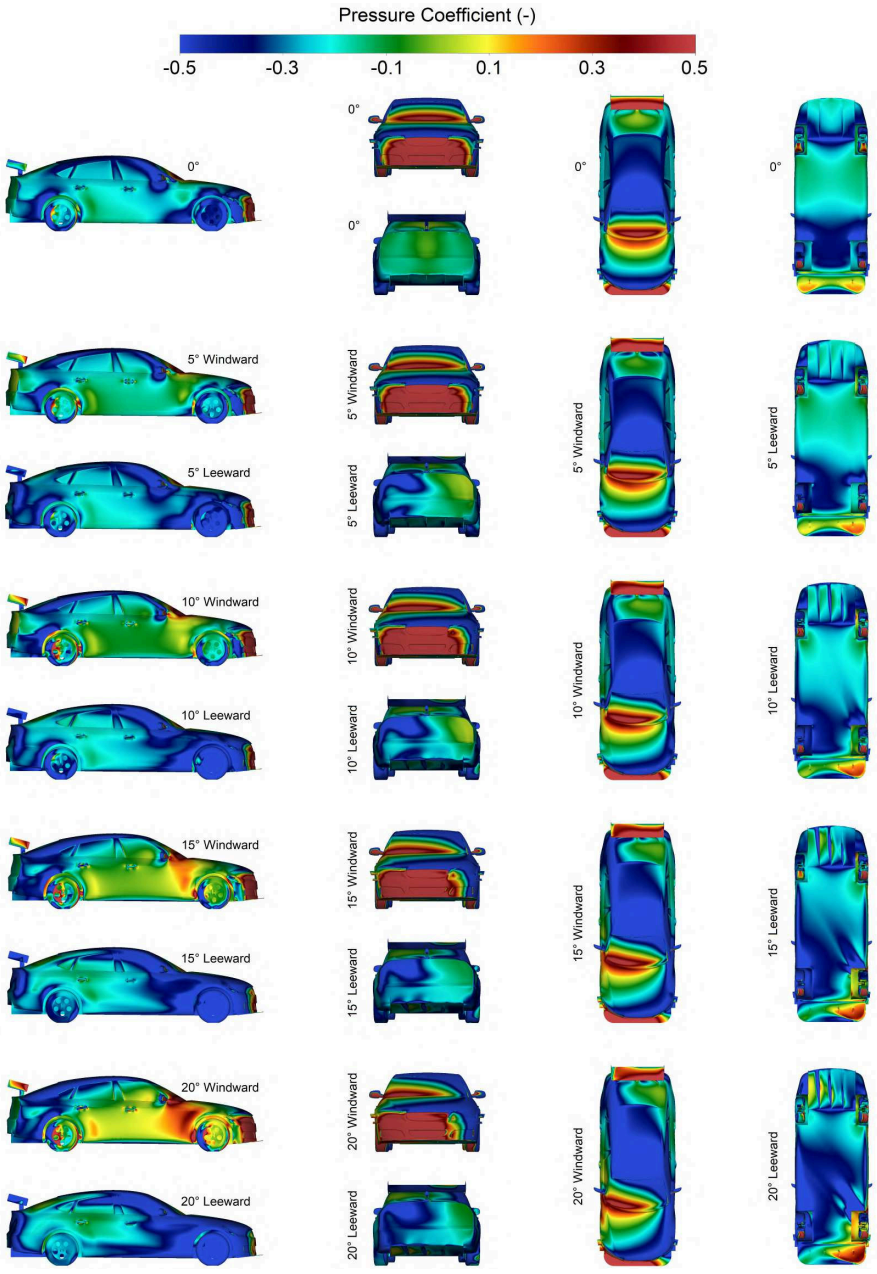

Figure 19: Numerical results of mean surface pressure coefficients C_p on the high-performance vehicle with rear wing configuration across the yaw angle range

4.3.2. Slant

Experimental measurement results of time-averaged surface pressure coefficients on the slant of the standard, spoiler, and rear wing configurations of the *DrivAer hp-F* model are presented in Figure 20. The standard configuration at 0° yaw depicts a pressure recovery from $C_p \approx$ -0.70 at the roof's trailing edge to $C_p \approx$ -0.26 downstream at the centre of the slant. The sides of the slant demonstrate a more gradual pressure recovery due to relatively high velocity airflow along the c-pillars. The yaw conditions cause airflow to be accelerated around the windward c-pillar and across the slant, as previously discussed in section 4.3.1. The resultant emerging low pressure region is observed around the top windward corner of the slant, and the general pressure recovery shifts with the direction of the freestream airflow. Consequently, the average pressure on the slant of the standard configuration reduces from $C_p \approx$ -0.38 at 0° yaw to $C_p \approx$ -0.52 at 20° yaw. The pressure maximum also reduces to $C_p \approx$ -0.32 at 20° yaw and is moved towards the bottom leeward corner.

The spoiler configuration exhibits an average pressure of $C_p \approx$ -0.23 across the slant at 0° yaw, which is about 40% higher than the standard configuration. This increase is attributed to the pressure build-up at the spoiler, which affects the pressure distribution upstream on the slant. The upstream effects persists towards the roof's trailing edge, shown by the local pressure increase over the standard configuration. Two local pressure maxima of $C_p \approx$ -0.16 occur at the downstream corners of the slant due to the interaction of the spoiler with high velocity airflow from the c-pillars. The yaw conditions cause the pressure maxima to shift with the direction of the high velocity airflow from the c-pillars, leading to the disappearance of the leeward pressure maximum at 10° yaw. The windward pressure maximum decreases to $C_p \approx -0.18$ and shifts towards the bottom leeward corner of the slant at 20° yaw. Similar to the standard configuration, an increasing low pressure region forms at the top windward corner, and the pressure recovery generally aligns with the direction of the freestream airflow. The average pressure across the slant decreases to $C_p \approx$ -0.44 at 20° yaw, which is approximately 16% higher than on the standard configuration due to upstream effects from the spoiler.

The rear wing configuration initially depicts a pressure distribution similar to the standard configuration at 0° yaw. The centralised pressure build-up is increased by the obstruction from the rear wing support, which therefore reaches a pressure maximum of $C_p \approx -0.17$. Unlike the spoiler configuration, upstream effects are less pronounced on the sides of the slant at 0° yaw because the rear wing does not provide a substantial pressure build-up in those regions. Consequently, the average total pressure across the slant is $C_p \approx -0.27$ at 0° yaw, which is only approximately 29% higher than the standard configuration. In yaw conditions, the pressure recovery aligns with the direction of the freestream airflow, and the pressure maximum forms an oval shape which stretches to the slant's centre. Section 4.3.3 will illustrate that the pressure recovery characteristics result from the interaction between the angled airflow and the rear wing's leading edge, which creates a higher pressure on the leeward side of the rear wing's upper surface. The upstream effects from the high pressure region on the rear wing lead to a maximum pressure of $C_p \approx -0.30$ at 20° yaw. Additionally, the rear wing configuration exhibits an average pressure of $C_p \approx -0.45$ on the slant at 20° yaw, which is approximately 14% higher than the standard configuration.

4.3.3. Rear Wing

Numerical results for time-averaged surface pressure coefficients on the upper and lower surface of the rear wing are shown in Figure 19. The upper surface displays a high pressure near the leading edge, which gradually decreases in magnitude towards the trailing edge at 0° yaw. Regions near the endplates exhibit a steeper pressure reduction, since they are affected by outboard rotating vortices which spill high pressure airflow to the freestream airflow. The yaw conditions cause a pressure reduction on the windward side of the upper surface, due to flow obstruction from the windward endplate. The obstruction and subsequent outboard pressure build-up on the windward endplate increase with yaw, as shown in Figure 19. This pressure build-up produces an inboard rotating vortex at large yaw angles, which creates the low pressure concentration near the windward endplate. The leeward side of the upper surface experiences less flow obstruction and therefore maintains higher pressures throughout the yaw angle range. Consequently, the upstream effects cause the leeward concentration of the pressure maximum on the slant, as discussed in section 4.3.2. Additionally, the pressure build-up on the inboard side of the leeward in yaw conditions causes the increasing pressure observed near the leeward endplate.

The lower surface exhibits a substantial low pressure region near the leading edge, followed by a steep pressure recovery downstream at 0° yaw. More gradual pressure recoveries are observed near the endplates, which are influenced by inboard rotating vortices that feed airflow onto the lower surface. The rear wing support hinders airflow acceleration around the leading edge and causes a small stagnation zone. In yaw conditions, the outboard pressure build-up at the windward endplate intensifies the inboard rotating vortex and consequently increases the low pressure concentration near the windward endplate. Furthermore, the airflow velocity along the windward c-pillar and slant increases with yaw, as discussed in sections 4.3.1 and 4.3.2, which aids the formation of the low pressure region observed on the windward side of the lower surface. The leeward side of the lower surface is predominantly affected by flow obstruction from the rear wing support. The obstruction at small yaw angles does not have detrimental effects on the pressure distribution yet, as observed at 5° yaw. However, the adverse effects from the obstruction from the rear wing support substantially increases the pressure along the leeward side of the lower surface at larger yaw angles. Additionally, the pressure build-up at the inboard side of the leeward endplate suppresses the formation of an inboard rotating vortex, resulting in the absence of a low pressure concentration near the leeward endplate.

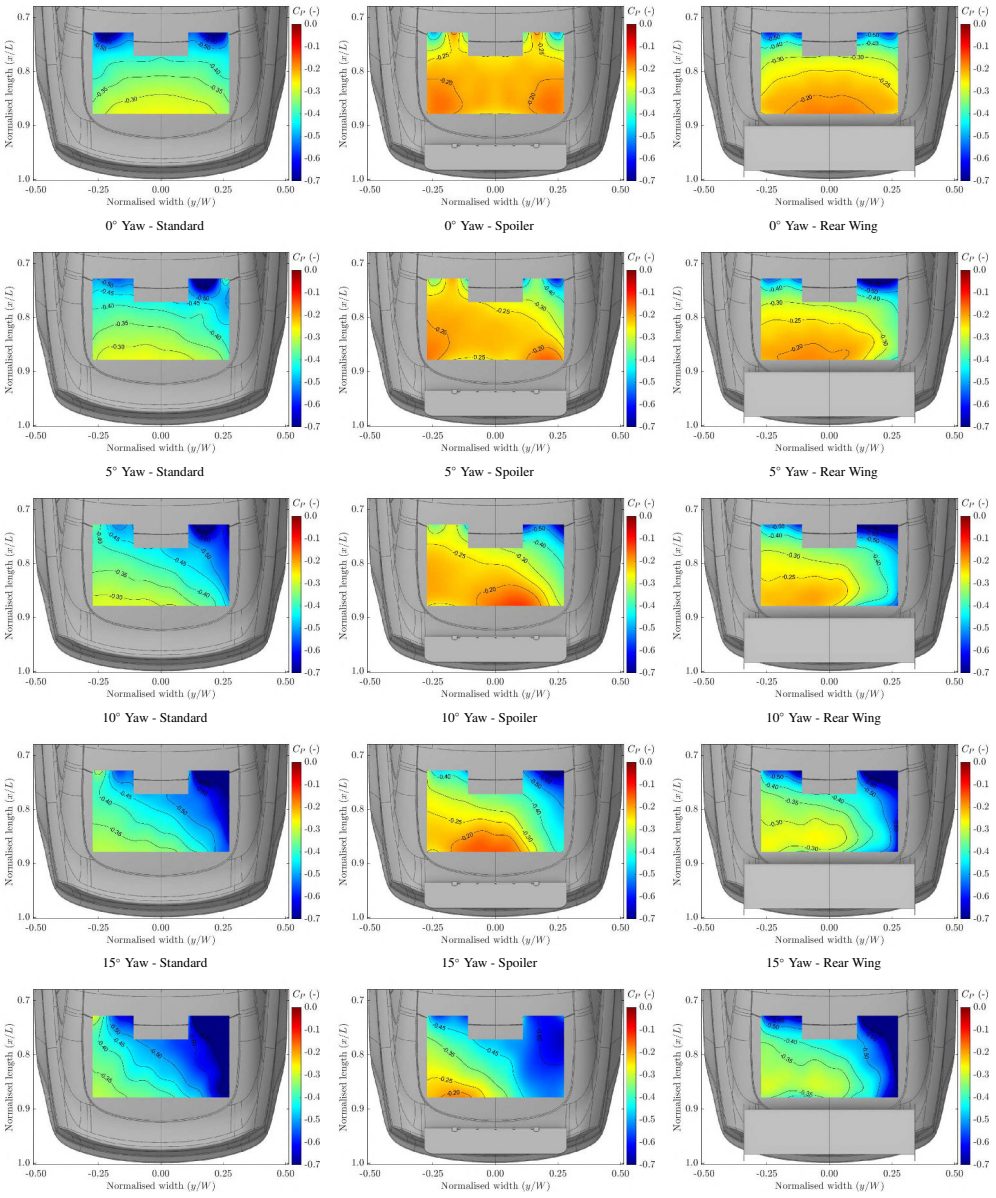

Figure 20: Experimental measurement results of time-averaged surface pressure coefficients C_p on the slant of the standard, spoiler, and rear wing high-performance vehicle configurations across the yaw angle range

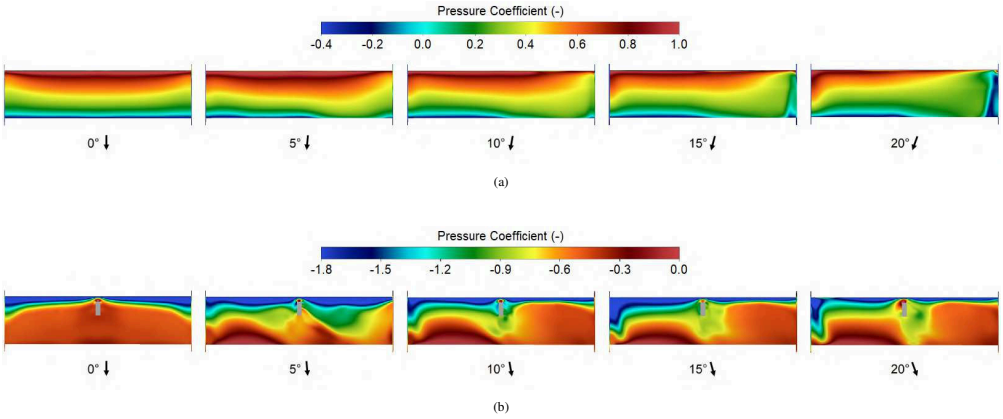

Figure 21: Numerical results of mean surface pressure coefficients C_p on the (a) upper and (b) lower surface of the rear wing across the yaw angle range

4.4. Wake Characteristics

This section analyses the wake characteristics at each yaw angle using the experimental measurement results of time-averaged total pressure coefficients on three wake planes behind the *DrivAer hp-F* model with rear wing configuration presented in Figure 22. The P1, P2 and P3 wake planes are positioned $0.25L$, $0.43L$ and $0.62L$ downstream of the vehicle model. The horizontal shift in the position of the main wake structure is a result of the vehicle rotation in the wind tunnel experiments.

4.4.1. 0° yaw

The main near-wake structure on the P1 plane generated by the vehicle in straight-line conditions is characterised by a square and mushroom-shaped region. The square-shaped wake region, which is approximately $1W$ wide and $0.75H$ tall, results from low energy airflow emerging from the vehicle's body. The mushroom-shaped upper wake region, which is about $0.75W$ wide and $0.3H$ tall, formed by vortical flow from the rear wing. Additional wake expansion, associated with rear wheel wakes and ground boundary layer flow, occurs along the wind tunnel floor around $y/W \approx \pm 0.55$.

The main wake characteristics of this high-performance vehicle model in straight-line conditions are dominated by upwash from the diffuser and vortical flow from the rear wing. Diffuser upwash is represented by the centralised circular trace of $C_{pT} \approx 0.10$ at $z/H \approx 0.30$. The counter-rotating vortex pair generated at the rear wing is located at $y/W \approx \pm 0.28$, $z/H \approx 0.83$. The interaction between these outboard rotating rear wing vortices produces lateral inwash of high energy freestream airflow and additional vertical upwash at the centre of the wake.

The downstream wake development on the P2 plane shows that the lateral inwash has reduced the wake width by $0.08W$. The vertical upwash combined with the diffusion of the rear wing vortices has also increased the wake height by approximately $0.09H$. The inwash and upwash wake characteristics support wake mixing as well. Consequently, the average total pressure coefficient of the main wake (expressed by the region of $C_{pT} < 0.75$) has increased from $C_{pT} \approx 0.26$ on the P1 plane to $C_{pT} \approx 0.35$ on the P2 plane.

The wake width on the P3 plane is reduced by an additional $0.12W$ over the P2 plane, resulting in a total wake width reduction of approximately 20% over the P1 plane. The wake height is increased by another $0.04H$ over the P2 plane, leading to a nearly 13% wake height increment over the P1 plane. The dissipation of pressure losses, promoted by the mixing of relatively high energy freestream airflow into the wake, has also increased the average total pressure of the main wake on the P1 plane by approximately 63% to $C_{pT} \approx 0.42$ on the P3 plane.

4.4.2. 5° yaw

The significant effect of yaw conditions on the wake characteristics is immediately apparent from the P1 plane at 5° yaw. The yaw conditions introduce the formation of a strong inboard rotating vortex on the windward side of the vehicle, as previously identified in section 4.2. This clockwise rotating vehicle body vortex is depicted by the region of $C_{pT} \approx$ -0.17 at $y/W \approx 0.12$, $z/H \approx 0.70$ on the P1 plane. The pressure build-ups on the endplates in yaw conditions, discussed in section 4.3.3, promote the formation of stronger vortical flow at the rear wing. The counter-clockwise rotating vortex at the windward side of the rear wing is located at $y/W \approx 0.36$, $z/H \approx 0.91$. The clockwise rotating vortex at the leeward side of the rear wing is positioned at $y/W \approx$ -0.20, $z/H \approx 0.78$.

The diffuser upwash effect is eliminated by the angled coming airflow and the inboard propagation of the windward wheel wakes across the diffuser ramp. The middle wake region is therefore dominated by low energy separated airflow of $C_{pT} \approx$ -0.15 and does not show any noticeable higher energy airflow trace. Furthermore, wake traces of a larger leeward a-pillar vortex become observable at $y/W \approx$ -0.36, $z/H \approx 0.58$. More wake

expansions occurs around y/W < -0.43 due to additional airflow separation along the leeward side of the vehicle. Generally, the main wake on the P1 plane at 5° yaw has an average total pressure coefficient of $C_{pT} \approx 0.21$, which is approximately 20% lower than on the P1 plane at 0° yaw.

The main wake characteristics are now driven by the dominant vehicle body vortex and the vortical flow from the rear wing. The strong clockwise circulation of the vehicle body vortex induces a clockwise motion onto the counter-rotating vortex pair from the rear wing. This displacement reduces the amount of lateral inwash generated by the windward rear wing vortex. However, the leeward rear wing vortex is fed by the co-rotation of the vehicle body vortex and consequently generates a stronger inwash effect.

These wake characteristics are also evident from the wake development on the P2 plane, where the tilt angle from the upper wake region is increased from 8° on the P1 plane to about 23° on the P2 plane. The strong inwash on the leeward side has reduced the wake width locally by $0.08W$, while the wake width has remained unchanged on the windward side. The inwash of relatively high energy freestream airflow has also supported pressure loss dissipation and increased the average total pressure by nearly 61% to $C_{pT} \approx 0.34$.

The tilt angle of the upper wake region is increased to about 34° on the P3 plane. The wake width is reduced by an additional $0.07W$ over the P2 plane, leading to a total 18% wake width reduction compared to the P1 plane. Dissipation of pressure losses has also resulted in a total average total pressure of $C_{pT} \approx 0.42$, which is an approximate 100% increase over the P1 plane.

4.4.3. 10° yaw

The low total pressure trace of $C_{pT} \approx$ -0.22, located at $y/W \approx 0.24$, $z/H \approx 0.73$ on the P1 plane, is associated with the vehicle body vortex. The approximate 30% reduction in total pressure magnitude of this trace compared to the P1 plane at 5° yaw indicates that the vortex has increased in strength. The increased vehicle body vortex strength is also evident from the strong induced motion on the upper wake region, which depicts a tilt angle of 17°. As a result, the windward rear wing vortex is positioned at $y/W \approx 0.43$, $z/H \approx 0.94$, and the leeward rear wing vortex at $y/W \approx$ -0.12, $z/H \approx 0.71$.

The wake trace from the leeward a-pillar vortex at $y/W \approx$ -0.36, $z/H \approx 0.56$ has become more prominent and has propagated further outboard compared to the 5° yaw results. In addition, the middle wake region demonstrates more pressure losses, due to increased flow separation at the diffuser and vehicle body. More flow separation along the leeward side of the vehicle has also caused a greater wake expansion at y/W < -0.40. Altogether, the main wake on the P1 plane has an average total pressure coefficient of $C_{pT} \approx 0.19$, which is nearly 10% lower than at 5° yaw.

The dominance of the strong vehicle body vortex on the wake characteristics is evident from the downstream development of the wake on the P2 plane. The upper wake region is induced with a clockwise motion, which has increased its tilt angle to 35°. The interaction of the co-rotating vehicle body vortex and leeward rear wing vortex does not only produce lateral inwash on the leeward side of the wake, but also generates a component of local vertical downwash in this region. The strong leeward inwash reduces the wake width by about $0.08W$ on the leeward side compared to the P1 plane. However, the strength of this one-sided inwash has increased compared to the 5° yaw case and creates a crossflow component throughout the wake. This crossflow produces a minor windward outwash effect, causing an approximate $0.03W$ windward wake width increase over the P1 plane. The leeward downwash effect has also decreased the wake expansion at y/W < -0.40 by about $0.08H$. In general, the main wake on the P2 plane demonstrates an average total pressure coefficient of $C_{pT} \approx 0.32$, which is approximately 67% higher than on the P1 plane.

The considerable circulation of the vehicle body vortex has increased the tilt angle of the upper wake region to about 53° on the P3 plane. The strong leeward inwash is also still evident on the P3 plane, which depicts an additional wake width reduction of $0.08W$ over the P2 plane on the leeward side of the wake. Moreover, the windward outwash effect has increased the windward wake width by an additional $0.02W$. The leeward downwash has decreased the wake expansion height at y/W < -0.40 by another $0.06H$ over the P2 plane. Altogether, the main wake width on the P3 plane is reduced by approximately 9% and the wake expansion height at y/W < -0.40 by about 36% compared to the P1 plane. The leeward inwash, windward outwash and leeward downwash wake characteristics have also promoted the dissipation of the pressure losses. The average total pressure coefficient of the main wake is therefore increased to $C_{pT} \approx 0.41$ on the P3 plane, which is an approximate 114% increment over the P1 plane.

4.4.4. 15° yaw

The vehicle body vortex on the P1 plane at 15° yaw is depicted by the wake trace of $C_{pT} \approx$ -0.33 at $y/W \approx 0.35$, $z/H \approx 0.71$. The approximate 50% reduction in total pressure magnitude of this wake trace compared to the 10° yaw case is again indicative of its increased strength. The positioning of the rear wing vortex pair is also indicative of a larger and stronger vehicle body vortex, since they have been induced further apart. Consequently, the leeward rear wing vortex is positioned at $y/W \approx 0.02$, $z/H \approx 0.69$ and its wake trace is almost detached from the main wake trace. The windward rear wing vortex is positioned at $y/W \approx 0.52$, $z/H \approx 0.94$, resulting in an upper wake tilt angle of about 30°.

The wake trace from the leeward a-pillar vortex at $y/W \approx$ -0.27, $z/H \approx 0.49$ starts to merge the wake expansion at y/W < -0.30 resulting from considerable flow separation along the leeward side of the vehicle. The pressure losses in the middle wake region have become more severe compared to the 10° yaw results, due to more flow separation at the diffuser and vehicle body. Overall, the main wake on the P1 plane depicts an average total pressure coefficient of $C_{pT} \approx 0.18$, which is approximately 7% lower than at 10° yaw.

The wake characteristics discussed for the 10° yaw results have intensified at 15° yaw. The clockwise motion induced by

the strong circulation from the vehicle body vortex onto the upper wake region has increased its tilt angle to about 43° on the P2 plane. The induced motion on the leeward rear wing vortex is especially evident, since the detached wake trace at the P1 plane is shifted downwards and inboard into the main wake trace on the P2 plane. Furthermore, while no substantial wake width reduction occurs on the leeward side of the wake due to the large declination of the main wake structure, the clockwise circulation produced by the vehicle body vortex and leeward rear wing vortex creates a substantial diagonal crossflow towards the top windward side of the wake. The resultant windward outwash effect has caused an approximate $0.04W$ windward wake width increase compared to the P1 plane. The leeward downwash has also reduced the height of the wake expansion at y/W < -0.30 by nearly $0.09H$. These dominant wake characteristics promote wake mixing and consequently increased the average total pressure in the main wake on the P2 plane to $C_{pT} \approx 0.31$, which is approximately 77% higher than on the P1 plane.

The tilt angle of the upper wake region is increased to around 60° at the P3 plane. Again, no noticeable wake width reduction is observed on the leeward side of the wake due to the large declination of the main wake structure. However, the strong diagonal crossflow and resultant windward outwash have increased the windward wake width by an additional $0.04W$ over the P2 plane, leading to a total windward wake with increase of about 14% compared to the P1 plane. The leeward downwash has decreased the wake expansion height at y/W < -0.30 by an additional $0.10H$ over the P2 plane, providing a total reduction of the wake expansion height of about 60% compared to the P1 plane. Generally, the strong wake characteristics have promoted the dissipation of pressure losses throughout the downstream wake planes. The main wake on the P3 plane therefore depicts an average total pressure coefficient of $C_{pT} \approx$, which is an approximate 125% increase over the P1 plane.

4.4.5. 20° yaw

The vehicle body vortex is represented by the wake trace of $C_{pT} \approx$ -0.35 at $y/W \approx 0.48$, $z/H \approx 0.70$ on the P1 plane. The larger wake trace and approximate 6% lower total pressure magnitude compared to the 15° yaw case indicates that this vortex has increased in size and strength. The strong circulation from the vehicle body vortex is also evident from its influence on the positioning of the rear wing vortices. The leeward rear wing vortex is positioned at $y/W \approx 0.04$, $z/H \approx 0.69$ and its wake trace is further disconnected from the main wake trace compared to at 15° yaw. The counter-clockwise rotating windward rear wing vortex is positioned at $y/W \approx 0.71$, $z/H \approx 0.95$.

However, an additional wake trace from a clockwise rotating vortex from the windward side of the rear wing's upper surface is observed at $y/W \approx 0.83$, $z/H \approx 0.93$. The formation of this additional windward rear wing vortex is a result of the pressure build-up at the outboard side of the windward endplate in yaw conditions, as discussed in section 4.3.3. It is expected that the pressure build-up at smaller yaw angles also creates this additional vortex, but with far less strength. This much weaker clockwise rotating vortex from the rear wing's upper surface would therefore quickly merge into the dominant counter-clockwise rotating vortex from the rear wing's lower surface and not leave an observable distinct wake trace on the windward side of the wake at smaller yaw angles.

The pressure losses in the middle wake region have qualitative only slightly increase, indicating no substantial additional flow separation from the diffuser and vehicle body. The leeward a-pillar vortex does not contain a distinct wake trace any more at 20° yaw, as its trace is completely merged into the wake expansion region at y/W < -0.15. The size and pressure losses in the wake expansion at y/W < -0.15 have increased over the 15° yaw case, due to additional flow separation along the leeward side of the vehicle. Altogether, the average total pressure coefficient of the main wake on the P1 plane is $C_{pT} \approx 0.15$, which is nearly 13% lower than at 15° yaw.

The results on the P2 plane show that the strong circulation from the vehicle body vortex remains the most dominant wake characteristic at 20° yaw. The resultant induced motion onto the upper wake region has increased its tilt angle from about 38° on the P1 plane to 56° on the P2 plane. Even tough the wake starts to develop outside the measurement zone on the downstream wake planes, it is estimated that the windward outwash effect created by the crossflow has increased the windward wake width by about $0.04W$. Similarly to the 15° yaw case, no noticeable leeward wake width reduction is created by the inwash on the leeward side, due to the large declination of the main wake structure. Yet, the leeward downwash effect has decreased the height of the wake expansion at y/W < -0.15 by nearly $0.09H$. In general, these wake characteristics promote wake dissipation and increased the average total pressure of the main wake to $C_{pT} \approx 0.28$ on the P2 plane, which is approximately 82% higher than on the P1 plane.

The tilt angle of the upper wake region is further increased to about 67° on the P3 plane. The strong diagonal crossflow and resultant windward outwash have increased the windward wake width by another estimated $0.04W$ compared to the P2 plane, leading to a total windward wake width increase of approximately 12% over the P1 plane. The downwash effect has decreased the height of the wake expansion region at y/W < -0.15 by an additional $0.08H$ over the P2 plane, resulting in a total height reduction of this wake region of approximately 33% compared to the P1 plane. Overall, the downstream dissipation of pressure losses have increased the average total pressure coefficient of the main wake on the P3 plane to $C_{pT} \approx 0.36$, which is an approximate 137% increment over the P1 plane.

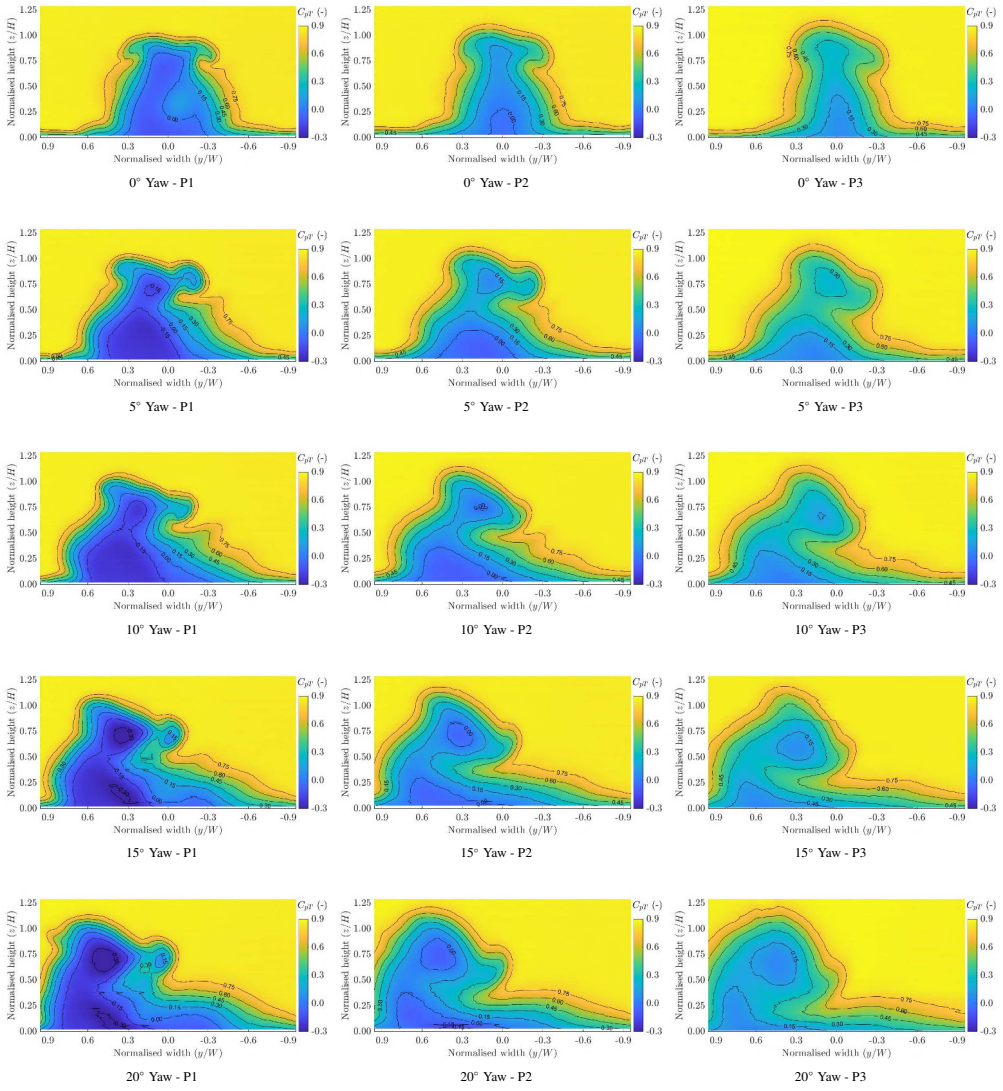

Figure 22: Experimental measurement results of time-averaged total pressure coefficients C_{pT} on the P1, P2 and P3 wake planes behind the high-performance with rear wing configuration across the yaw angle range

5. Conclusions

This paper studied the effects of yaw conditions on the aerodynamic performance and flow field of high-performance vehicles through measurements of aerodynamic forces, surface pressure on the slant, and total pressure in the wake of the *DrivAer hp-F* model in the 8x6 Wind Tunnel at Cranfield University. Additionally, complementary numerical results were presented to support the interpretation of the experimental data and facilitate a more comprehensive discussion on the effects of yaw conditions.

Aerodynamic force measurements on the standard, spoiler, and rear wing configurations of the *DrivAer hp-F* model revealed that the standard configuration generates minor front axle downforce and substantial rear axle lift in straight-line conditions. The yaw conditions generally caused a slight downforce increase on the leeward wheels but a more significant lift increase on the windward wheels. The spoiler and rear wing devices increased front axle lift and rear axle downforce compared to the standard configuration. The rear wing configuration generated approximately 50% more additional downforce over the spoiler configuration. However, the rear wing also demonstrated the highest yaw sensitivity due to downforce losses from significant flow obstruction from the windward endplate. Additionally, the yaw conditions caused a non-linear increase in drag for each vehicle configuration. The spoiler and rear wing configurations generated approximately 6% and 11% more drag than the standard configuration across the yaw angle range. Nonetheless, the rear wing configuration still proved to be the most aerodynamically efficient at each yaw angle. Moreover, the yaw conditions increased side force in the leeward direction fairly linearly. The larger side profile of the spoiler and rear wing configurations caused a maximum increase in side force coefficients of approximately 5% and 16% over the standard configuration at 20° yaw.

Yaw conditions also had a substantial impact on the vehicle's flow field and pressure distribution. Wheel wakes started to propagate in the direction of the freestream airflow, causing significant interference effects along the underbody and outboard flow separation along the leeward side of the vehicle. Furthermore, flow velocities around curvatures at the windward side of the vehicle such as the a-pillar, c-pillar and roof were increased and considerably contributed to the lift increase across the yaw angle range. These flow conditions also had a significant impact on the downstream flow behaviour on the slant, which was experimentally confirmed by measurements of surface pressure on the slant. The experimental data showed that the pressure recovery along the slant, together with the local pressure maximum, shifted with the direction of the freestream airflow in yaw conditions. An emerging low pressure region was created around the top windward corner, and the average pressure along the entire slant reduced at increasing yaw angles. Moreover, upstream effects from the spoiler and rear wing devices had a substantial impact on the pressure distribution along the slant and persisted towards the roof's trailing edge. The pressure distribution on the rear wing itself also demonstrated a high sensitivity to yaw conditions due to changes in vortical flow, and flow obstruction from the endplates and rear wing support.

Measurements of total pressure coefficients on wake planes behind the *DrivAer hp-F* model with rear wing configuration revealed that the straight-line wake characteristics were dominated by diffuser flow and vortical flow from the rear wing, which combined created a strong outboard inwash and centre upwash effect. In yaw conditions, a dominant inboard rotating vortex was created behind the windward side of the vehicle, which increased in size and strength across the yaw angle range. Airflow on the leeward side of the vehicle rolled-up into spanwise recirculation wake vortices and created significant pressure reductions on the vehicle's base. The interaction between the windward vehicle body vortex and vortical flow from the rear wing primarily created a strong leeward inwash at small yaw angles. The increased circulation from the vehicle body vortex at larger yaw angles caused the entire main wake structure to tilt leewards. The leeward inwash effect intensified and produced a strong diagonal crossflow which caused some windward outwash. The strong circulation also generated a component of leeward downwash onto the wake expansion region. Generally, these wake characteristics promoted wake mixing and consequently increased the dissipation rate of pressure losses across the yaw angle range.

Overall, this study has extended the knowledge on the effects of yaw conditions on vehicle aerodynamics into the high-performance space. The presented findings form a solid base for future work to extend the analyses to other real-world operating conditions for high-performance vehicles. Furthermore, the presented experimental data broadens the limited database of wind tunnel data for aerodynamic research on high-performance vehicles.

Acknowledgements

The authors would like to thank the technicians from the 8x6 Wind Tunnel at Cranfield University for their valuable support during the extensive wind tunnel campaign.

Conflict of Interest Statement

The authors have no conflicts to disclose.

Data Availability Statement

The data that support the findings of this study are available within the article.

References

[1] A. M. Althaf, Y. S. Bangaru, R. Fawcett, V. M. Guled, T. G. Maloo, P. N. Gorgojo, C. R. Sala, A. S. Felix, T.-R. Teschner, T. I. Józsa, A. Borgoltz, N. Intaratep, W. J. Devenport, and M. Szoke. Numerical modeling and tunnel specific considerations for cfd model development of low-speed wind tunnels. *AIAA AVIATION 2023 Forum*, 2023. doi: https://doi.org/10.2514/6.2023-3980.

[2] ANSYS, Inc. *ANSYS Fluent Theory Guide*. Canonsburg, PA, USA, 2009. https://www.afs.enea.it/project/neptunius/docs/fluent/html/th/node1.htm.

[3] F. Bello-Millán, T. Mäkelä, L. Parras, C. del Pino, and C. Ferrera. Experimental study on ahmed's body drag coefficient for different yaw angles. *Journal of Wind Engineering and Industrial Aerodynamics*, 157:140–144, 2016. ISSN 0167-6105. doi: https://doi.org/10.1016/j.jweia.2016.08.005.

[4] A. Booysen, P. Das, and S. Ghaemi. Large-scale 3d-ptv measurement of ahmed-body wake in crossflow. *Experimental Thermal and Fluid Science*, 132:110562, 2022. ISSN 0894-1777. doi: https://doi.org/10.1016/j.expthermflusci.2021.110562.

[5] A. Buljac, I. Džijan, I. Korade, S. Krizmanić, and H. Kozmar. Automobile aerodynamics influenced by airfoil-shaped rear wing. *International Journal of Automotive Technology*, 17(3):377–385, 2016. doi: https://doi.org/10.1007/s12239-016-0039-4.

[6] S.-Y. Cheng, K.-Y. Chin, S. Mansor, and A. B. Abd Rahman. Experimental study of yaw angle effect on the aerodynamic characteristics of a road vehicle fitted with a rear spoiler. *Journal of Wind Engineering and Industrial Aerodynamics*, 184:305–312, 2019. ISSN 0167-6105. doi: https://doi.org/10.1016/j.jweia.2018.11.033.

[7] C. M. Freeman and A. P. Gaylard. Correlation of cfd simulation for front side glass wall pressure fluctuations at yaw. *8th MIRA International Vehicle Aerodynamics Conference*, 2010.

[8] K. P. Garry and G. M. Le Good. An investigation of the sensitivity of rear wing orientation for saloon race cars. In *SAE 2005 World Congress & Exhibition*. SAE International, apr 2005. doi: https://doi.org/10.4271/2005-01-1018.

[9] D. Gogel and H. Sakurai. The effects of end plates on downforce in yaw. In *Motorsports Engineering Conference & Exposition*. SAE International, dec 2006. doi: https://doi.org/10.4271/2006-01-3647.

[10] M. Grandemange, O. Cadot, A. Courbois, V. Herbert, D. Ricot, T. Ruiz, and R. Vigneron. A study of wake effects on the drag of ahmeds square-back model at the industrial scale. *Journal of Wind Engineering and Industrial Aerodynamics*, 145:282–291, 2015. ISSN 0167-6105. doi: https://doi.org/10.1016/j.jweia.2015.03.004.

[11] A. Heft, T. Indinger, and N. Adams. Introduction of a new realistic generic car model for aerodynamic investigations. *SAE Technical Paper 2012-01-0168*, 04 2012. doi: 10.4271/2012-01-0168.

[12] J. Howell. Aerodynamic drag of passenger cars at yaw. *SAE International Journal of Passenger Cars—Mechanical Systems*, 8(1):306–316, 2015. ISSN 1946-4002. doi: https://doi.org/10.4271/2015-01-1559.

[13] J. J. Newbon, R. R. Dominy, and D. Sims-Williams. Cfd investigation of the effect of the salient flow features in the wake of a generic open-wheel race car. *SAE International Journal of Passenger Cars—Mechanical Systems*, 8(1):217–232, 2015. ISSN 1946-4002. doi: https://doi.org/10.4271/2015-01-1539.

[14] J. Katz and R. Largman. Experimental study of the aerodynamic interaction between an enclosed-wheel racing-car and its rear wing. *Journal of Fluids Engineering*, 111(2):154–159, 06 1989. ISSN 0098-2202. doi: https://doi.org/10.1115/1.3243616.

[15] J. Keogh. *The Aerodynamic Effects of the Cornering Flow Conditions*. PhD thesis, School of Mechanical and Manufacturing Engineering, University of New South Wales, 2016.

[16] J. Keogh, G. Doig, S. Diasinos, and T. Barber. The influence of cornering on the vortical wake structures of an inverted wing. *Proceedings of the Institution of Mechanical Engineers, Part D: Journal of Automobile Engineering*, 229(13):1817–1829, 2015. doi: 10.1177/0954407015571673.

[17] C. Lai, S. Zhu, S. Feng, G. Zhai, L. Tan, and S. Obayashi. Flow characteristics and wake topology of two-seat convertibles. *Physics of Fluids*, 35(1):015144, 2023. ISSN 1070-6631. doi: 10.1063/5.0134090.

[18] M. Lanfrit. Best practice guidelines for handling automotive external aerodynamics with fluent. 2005. Fluent Deutschland GmbH.

[19] M. Lorite-Díez, J. Jiménez-González, L. Pastur, O. Cadot, and C. Martínez-Bazán. Drag reduction on a three-dimensional blunt body with different rear cavities under cross-wind conditions. *Journal of Wind Engineering and Industrial Aerodynamics*, 200:104145, 2020. ISSN 0167-6105. doi: https://doi.org/10.1016/j.jweia.2020.104145.

[20] A. Mathur, A. Mahajan, A. Aggarwal, C. Mishra, and A. Roy. Numerical study of swan neck rear wing for enhancing stability of ground vehicle bodies. In *Emerging Trends in Mechanical Engineering*, pages 199–208, Singapore, 2021. Springer Singapore. doi: https://doi.org/10.1007/978-981-15-8304-9_14.

[21] B. McAuliffe, B. Sowmianarayanan, and H. Barber. Near-to-far wake characteristics of road vehicles part 1: Influence of ground motion and vehicle shape. *SAE International Journal of Advances and Current Practices in Mobility*, 3(4):2025–2045, 2021. ISSN 2641-9645. doi: https://doi.org/10.4271/2021-01-0957.

[22] B. McAuliffe, B. Sowmianarayanan, and H. Barber. Near-to-far wake characteristics of road vehicles part 2: Influence of cross winds and free-stream turbulence. *SAE International Journal of Advances and Current Practices in Mobility*, 3(4):2009–2024, 2021. ISSN 2641-9645. doi: https://doi.org/10.4271/2021-01-0949.

[23] W. Meile, T. Ladinek, G. Brenn, A. Reppenhagen, and A. Fuchs. Non-symmetric bi-stable flow around the ahmed body. *International Journal of Heat and Fluid Flow*, 57:34–47, 2016. ISSN 0142-727X. doi: https://doi.org/10.1016/j.ijheatfluidflow.2015.11.002.

[24] F. R. Menter. Two-equation eddy-viscosity turbulence models for engineering applications. *AIAA Journal*, 32, 1994.

[25] Y. Nakamura, T. Nakashima, C. Yan, K. Shimizu, T. Hiraoka, H. Mutsuda, T. Kanehira, and T.Nouzawa. Identification of wake vortices in a simplified car model during significant aerodynamic drag increase under crosswind conditions. *Journal of Visualization*, 25:983–997, 2022. doi: https://doi.org/10.1007/s12650-022-00837-8.

[26] C. N. Nayeri, D. Wieser, H. J. Schmidt, C. Strangfeld, and O. C. Paschereit. Experiments on the influence of yaw on the aerodynamic behaviour of realistic car geometries. 2014. URL `https://api.semanticscholar.org/CorpusID:107534051`.

[27] J. Newbon, D. Sims-Williams, and R. Dominy. Aerodynamic analysis of grand prix cars operating in wake flows. *SAE International Journal of Passenger Cars—Mechanical Systems*, 10(1):318–329, 2017. ISSN 1946-4002. doi: https://doi.org/10.4271/2017-01-1546.

[28] S. Rijns, T.-R. Teschner, K. Blackburn, and J. Brighton. Aerodynamic analysis of the ride height dependency of a high-performance vehicle equipped with a multichannel diffuser in ground effect. *SAE Technical Paper 2023-01-5064*, 2023. ISSN 2688-3627. doi: https://doi.org/10.4271/2023-01-5064.

[29] S. Rijns, T.-R. Teschner, K. Blackburn, and J. Brighton. Integrated numerical and experimental workflow for high performance vehicle aerodynamics. *SAE Technical Paper 2024-01-5016*, 2024. doi: https://doi.org/10.4271/2024-01-5016.

[30] S. Satheesh, L. Cordier, F. Kerhervé, and A. Spohn. Yawed ahmed body: Impact of vertical flaps on flow structures. *12th International Symposium on Turbulence and Shear Flow Phenomena*, 2022.

[31] R. F. Soares. *Wake Characterisation and Simulation for Ground Vehicles*. PhD thesis, School of Aerospace, Manufacturing and Transport, Cranfield University, 2020.

[32] R. F. Soares, A. Knowles, S. G. Olives, K. Garry, and J. C. Holt. On the aerodynamics of an enclosed-wheel racing car: An assessment and proposal of add-on devices for a fourth, high-performance configuration of the drivaer model. *SAE Technical Paper 2018-01-0725*, April 2018. doi: https://doi.org/10.4271/2018-01-0725.

[33] C. Strangfeld, D. Wieser, H. Schmidt, R. Woszidlo, C. Nayeri, and C. Paschereit. Experimental study of baseline flow characteristics for the realistic car model drivaer. *SAE Technical Paper 2013-01-1251*, 2013. doi: https://doi.org/10.4271/2013-01-1251.

[34] X. Su, K. He, K. Xu, G. Gao, and S. Krajnović. Comparison of flow characteristics behind squareback bluff-bodies with and without wheels. *Physics of Fluids*, 35(3):035114, 2023. ISSN 1070-6631. doi: 10.1063/5.0138305.

[35] M. Szudarek and J. Piechna. Cfd analysis of the influence of the front wing setup on a time attack sports car's aerodynamics. *Energies*, 14(23), 2021. ISSN 1996-1073. doi: https://doi.org/10.3390/en14237907.

[36] T. The Hung, M. Hijikuro, M. Anyoji, T. Uchida, T. Nakashima, and K. Shimizu. Deflector effect on flow behavior and drag of an ahmed body under crosswind conditions. *Journal of Wind Engineering and Industrial Aerodynamics*, 231:105238, 2022. ISSN 0167-6105. doi: https://doi.org/10.1016/j.jweia.2022.105238.

[37] T. Tunay, E. Firat, and B. Sahin. Experimental investigation of the flow around a simplified ground vehicle under effects of the steady crosswind. *International Journal of Heat and Fluid Flow*, 71:137–152, 2018. ISSN 0142-727X. doi: https://doi.org/10.1016/j.ijheatfluidflow.2018.03.020.

[38] M. Urquhart. *Vehicles Wake in Side Wind*. PhD thesis, Department of Mechanics and Maritime Sciences,Chalmers University of Technology, 2021.

[39] H. Viswanathan. Aerodynamic performance of several passive vortex

generator configurations on an ahmed body subjected to yaw angles. *Journal of the Brazilian Society of Mechanical Sciences and Engineering*, 43: 131, 2021. doi: https://doi.org/10.1007/s40430-021-02850-8.

[40] M. Watts and S. Watkins. Aerodynamic structure and development of formula 1 racing car wakes. *SAE International Journal of Passenger Cars—Mechanical Systems*, 7(3):1096–1105, 2014. ISSN 1946-4002. doi: https://doi.org/10.4271/2014-01-0600.

[41] D. Wieser, H.-J. Schmidt, S. Müller, C. Strangfeld, C. Nayeri, and C. Paschereit. Experimental comparison of the aerodynamic behavior of fastback and notchback drivaer models. *SAE International Journal of Passenger Cars—Mechanical Systems*, 7(2):682–691, 2014. ISSN 1946-4002. doi: https://doi.org/10.4271/2014-01-0613.

[42] D. Wieser, C. N. Nayeri, and C. O. Paschereit. Wake structures and surface patterns of the drivaer notchback car model under side wind conditions. *Energies*, 13(2), 2020. ISSN 1996-1073.

[43] M. R. Wilson, R. G. Dominy, and A. Straker. The aerodynamic characteristics of a race car wing operating in a wake. *SAE International Journal of Passenger Cars—Mechanical Systems*, 1(1):552–559, 2009. ISSN 1946-4002. doi: https://doi.org/10.4271/2008-01-0658.

[44] Y. Yang and L. Zheng. Assessment of nonlinear-low reynolds number/detached eddy simulation turbulence model for wake flow field simulation of a realistic automotive model. *Physics of Fluids*, 35(1):015133, 2023. ISSN 1070-6631. doi: 10.1063/5.0129918.

[45] Z. Yuan, Z. Gu, Y. Wang, and X. Huang. Numerical investigation for the influence of the car underbody on aerodynamic force and flow structure evolution in crosswind. *Advances in Mechanical Engineering*, 10(10), 2018. doi: https://doi.org/10.1177/1687814018797506.

Experimental and numerical investigation of the aerodynamic characteristics of high-performance vehicle configurations under yaw conditions

Rijns, Steven

2024-04-05

Rijns S, Teschner TR, Blackburn K, et al., (2024) Experimental and numerical investigation of the aerodynamic characteristics of high-performance vehicle configurations under yaw conditions. Physics of Fluids, Volume 36, Issue 4, April 2024, Article number 045112
https://doi.org/10.1063/5.0196979